RYERSON UNIVERSITY
FACULTY OF ENGINEERING, ARCHITECTURE AND SCIENCE

DEPARTMENT OF AEROSPACE ENGINEERING

Design of Electrically Powered Morphing Winglet

Kunj Mistry

AER870 Aerospace Engineering Thesis – Final Report

Faculty Advisor: Dr. Fengfeng (Jeff) Xi

Date: April 16, 2021

Acknowledgements

The author would like to thank Dr. Fengfeng (Jeff) Xi for initiating and guiding the author through this project. The author would also like to thank V-Bond lee for providing valuable information based on his experience and expertise. Finally, the author would like to thank his sister, Aditi Mistry, for helping with the formatting and proof reading of this report.

Abstract

Cycloidal and planetary gear drives are considered for the actuation of an electrically powered morphing winglet. A torque of 6723 N*m is required at the winglet hinge. The stepper motor selected as the electrical actuator is the HT34-487 stepper motor. This motor can provide a torque of approximately 6 N*m. The cycloidal drive consists of the selected stepper motor, a bevel gearbox, and a two-stage cycloidal gearbox. The bevel gearbox is used to change the axis of rotation of the stepper motor from span-wise direction to chord-wise direction. Stage one of the cycloidal gearbox contains an input shaft, two cycloidal disks with 180 degrees offset rotation, an eccentric cam and an output shaft. The cycloidal disks in stage one have 35 lobes, providing a gear ratio of 35:1. The second stage of the cycloidal gearbox consists of only one cycloidal disk with 34 lobes, providing a gear ratio of 34:1. The total gear ratio of the cycloidal drive is 1190:1. Material selection and FEA simulations are performed on the components in the cycloidal drive to ensure the selected materials can withstand the applied loads. A differential planetary gear drive is also considered to actuate an electrically powered morphing winglet. Spur gears are selected to be used as the sun and planet gears. A ratio of 180:1 is achieved in the planetary gear drive. Using gear tooth bending calculators, it is found that designing spur gears to withstand the loads of the electrically powered morphing winglet and to fit inside the dimensions of the wingbox is not feasible.

Table of Contents

Nomenclature

Symbol:	Meaning:
B	Cycloidal disk thickness.
d	Diameter.
d_c	Diameter of fixed ring pins.
e_0	eccentricity
$F_{s,max}$	Maximum normal force acting on output pins.
L	Characteristic length for an equation.
m	Module.
N	Number of cycloidal disks in the stage.
N_p	Number of planets.
P	Load.
R_a	Radius of addendum circle.
R_b	Radius of base circle.
R_d	Radius of dedendum circle.
R_p	Radius of pitch circle.
r_2	Radius of pitch circle of fixed ring pins.
$r_{pin\ circle}$	Radius of output pin center location on the cycloidal disk.
T	Torque.
$T_{g_n c_n}$	Torque per cycloidal disk.
u	Gear ratio.
W	Cross-section constant of output pins.
X_w	X coordinates of the working profile of the cycloidal disk.
x	Coefficient of modification.

Y_w	Y coordinates of the working profile of the cycloidal disk.
z	Number of teeth.
z_1	Number of teeth on the cycloidal disk
z_2	Number of fixed ring pins.
z_w	Number of output pins in the stage.
δ	Distance between cycloidal disks.
σ	Stress.
φ	Parameter for the equations of X_w and Y_w.

Subscripts

1	Value of first stage of cycloidal gear
2	Value of second stage of cycloidal gear
$2a$	Value of planet gear that mesh with the stationary ring gear.
$2b$	Value of planet gear that mesh with the rotating ring gear.
$3a$	Value of stationary ring gear.
$3b$	Value of rotating ring gear.
H	Hinge
in	Input value
max	Maximum value
n	Value of nth stage
p	pin
sun	Value of sun gear.
$yield$	Yield value

Acronyms

DPGD	Differential Planetary Gear Drive
FEA	Finite Element Analysis
MA	Mechanical advantage
R.R	Reduction Ratio

Glossary

Cant angle	Angle between winglet and wing.
Morphlet	A winglet that can change one or more geometric properties during flight.

List of Figures

List of Tables

1. Introduction

1.1. Introduction to Winglets

Due to the increase in fuel prices during the 1970's fuel crises, new aircraft technology needed to be developed and employed to reduce aircraft fuel consumptions. Dr. Richard Whitcomb, a noted aeronautical engineer at the NASA Langley Research Center, reintroduced and refined the winglet [1]. He predicted that employing winglets to the wingtips of aircrafts would improve cruising efficiencies by six to nine percent. Winglets are defined as extensions of an aircraft's wingtips in a plane perpendicular to that of the wing.

Figure 1.1: Winglet on KC-135 test aircraft, with tufts displaying flow of air over winglet surface [1].

Figure 1.1 shows a winglet on a KC-135 test aircraft used to test the efficacy of winglets.

1.2. Benefits of Winglets

Based on the geometry of a wing, as an aircraft moves through the atmosphere, pressure differences are created on the top and bottom surfaces. The bottom surface is subject to a higher pressure than the top surface of the wing, which creates a net upwards force, called lift, allowing the aircraft to fly. Because of this pressure difference, however, at the wingtips of the aircraft (as well as over the entire wing) high pressure air can "bleed" over from the bottom surface of the wing to the top surface of the wing. This creates a trailing vortex and leads to a loss in lift force generation and an increase in induced drag.

Figure 1.2: Trailing wingtip vortex created by an aircraft [2].

Figure 1.2 shows a trailing vortex created by an aircraft. Introducing a winglet interferes with and reduces the effects of vortices at the wingtip. There, employing a winglet helps reduce drag, reduce fuel consumption, and allow a higher cruising range.

By conducting wind-tunnel testing and performing empirical research on a military version of the Boeing 707 jetliner test aircraft the winglet flight test program at the NASA Dryden Flight Research Center validated Dr. Richard Whitcomb's claims and recorded a 6.5 percent increase in the fuel mileage rate [1]. Consequently, winglets or other forms of wingtip devices that improve aircraft performance have been utilized in nearly all contemporary commercial aircrafts.

1.3. Introduction to Morphing Winglets

A morphing winglet, also known as a morphlet, is a winglet that can change one or more of its geometric properties during flight. Morphlets are a new and promising technology in civil aviation with advantages including increased fuel efficiency, improved aerodynamic characteristics and improved flight performance.

An existing type of morphlet developed by Boeing are winglets that pivot about an axis parallel to the yaw axis of the aircraft [3].

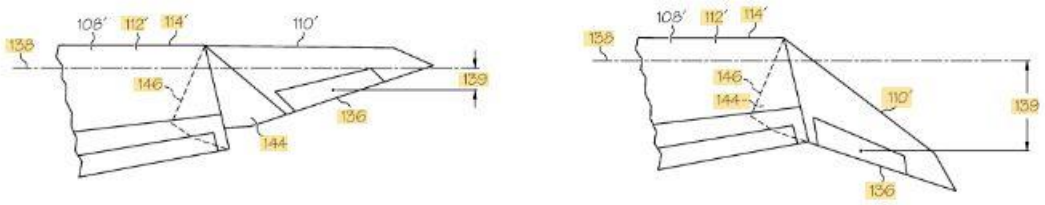

Figure 1.3: Adjustable winglet development by Boeing [3].

Figure 1.3 shows the basic motion of the morphlet developed by Boing. Outboard ailerons, as seen in Figure 1.3, are also included on the morphlet for improved control of the aircraft.

Moreover, a morphlet can also be designed to change its cant angle. The cant angle of a winglet is defined as the angle between the winglet and the main body of the wing (or section of wing at which the winglet is attached if the wing is polyhedral).

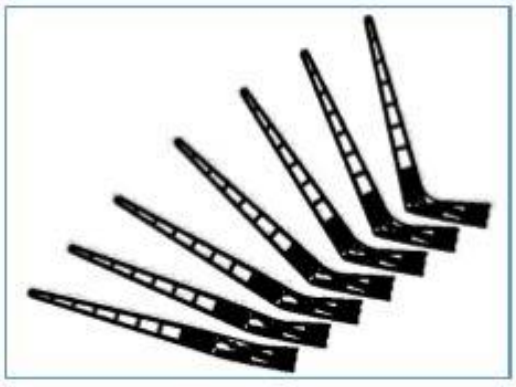

Figure 1.4: Cant motion of a morphlet [4].

Figure 1.4 shows the cant motion of a morphlet. Controlling the cant angle of a winglet can also lead to significant fuel savings. The scope of this design project pertains to only controlling the cant motion of the morphlet of an aircraft.

1.4. Benefits of Morphing Winglets

As previously mentioned, winglets help reduce drag, fuel consumption, and allow a longer cruising range. However, winglets utilized on modern-day commercial aircrafts are optimized for all phases of a flight mission, instead of being optimized for each individual phase. This inherently leads to

inefficiencies because during a phase of a flight mission the winglet will not perform as well as a winglet optimized for the current phase would.

On the other hand, the geometry of a morphlet can be adjusted and optimized in flight for each phase of a flight mission. The improvements in specific air range, distance traveled per mass of fuel burned, have been estimated to be four to five percent when a morphlet is applied to an aircraft, rather than a standard fixed winglet [5].

1.5. Current Morphing Winglet Mechanisms

A mechanism designed by Ryerson University graduates, titled Analysis and Control of An Actuation-Redundant Parallel Mechanism Requiring Synchronization, utilizes a pair of linear actuator and linkage systems to change the cant angle of a morphlet.

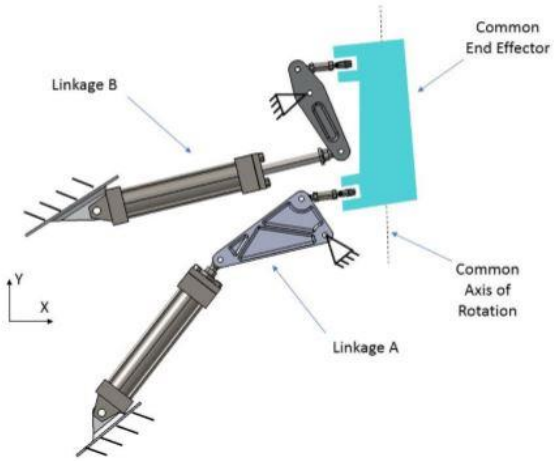

Figure 1.5: Linear actuator and linkage system for morphlet [4].

Figure 1.5 shows the linkage and linear actuator system designed by Ryerson University graduates. The drawback of this system, however, is the use of the linear actuators. The suggested linear actuators, electro-mechanical and hydraulic, need extra components to enable position recognition and control. This decreases the amount of achievable precision of the cant angle of a morphlet.

Moreover, a conceptual design utilizing compliant mechanisms for the morphlet is discussed in a paper titled ‘Conceptual study of a morphing winglet based on unsymmetrical stiffness’, written by C.

Wang, H. Khodaparast and M. Friswell, for the ‘Aerospace Science and Technology’ journal. However, the uncertainty of compliant mechanisms for the use in the aerospace industry introduces doubt for this design. Also, like the design developed by Ryerson University graduates, this system uses linear actuators to change the cant angle of the morphlet.

1.6. Design Problem

Hydraulic actuators are used in existing designs of morphlet mechanisms because they provide a high power and load rating. This is important to overcome the high loads acting on a morphlet while an aircraft is in flight. However, as mentioned before, the achievable position accuracy as well as the efficiency of hydraulic actuators is low [6, 7]. Therefore, for the design pertaining to this report an electrical rotary actuator is considered.

Unlike hydraulic actuators, electrical actuators use electrical power to drive the actuation. Electrical actuators have better positioning capabilities and velocity control that allow for synchronization [7]. Moreover, electrical actuators also have high efficiency, low operating costs and require low maintenance.

There are many types of electrical actuators available on the market for aerospace applications. The two that are considered for the actuation of a morphlet for this report are: servo motors and stepper motors. Servo motors are actuators that offer precise angular and angular velocity control. However, servo motors offer relatively low torque output while being expensive [8]. Stepper motors make use of a cogged stator and rotor design to control the angle the motor travels based on the space between stators [9]. Stepper motors are lower cost and have higher torque ratings compared to servo motors but sacrifice the precise angular control that servo motors offer.

2. Proposed Designs

The cross-sectional area of the wingbox determines the size, and hence the maximum torque, of the motor selected. To select an appropriate motor an online catalog on electromate.com is considered. The motor selected for the designs in this report is the HT34-487 stepper motor. Within the catalog on electromate.com this motor provides the highest torque and abides by the space constraints of the wingbox.

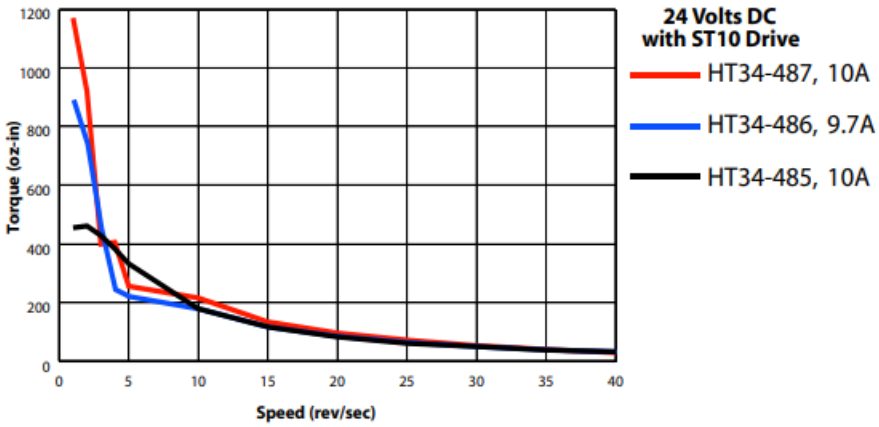

Figure 2.1: Torque - speed curve of HT34-487 motor [10].

Shown by the red curve in Figure 2.1, the available maximum continuous torque of the HT34-487 stepper motor at 24 Volts DC is around 1000 oz-in, which is equivalent to approximately 7 N*m, and the corresponding speed is approximately 3 rps. The values of torque and speed used to produce the gearbox designs is 6 N*m and 3 rps, respectively. Figure 7.1 given in Appendix A shows the torque – speed curve of the HT34-487 stepper motor at 48 Volts DC.

2.1. Constraints

Previously performed load analysis can be used to determine the maximum torque requires at the morphlet hinge. Figure 2.2 shows a diagram of the morphlet and the equivalent force vector acting on the center of pressure.

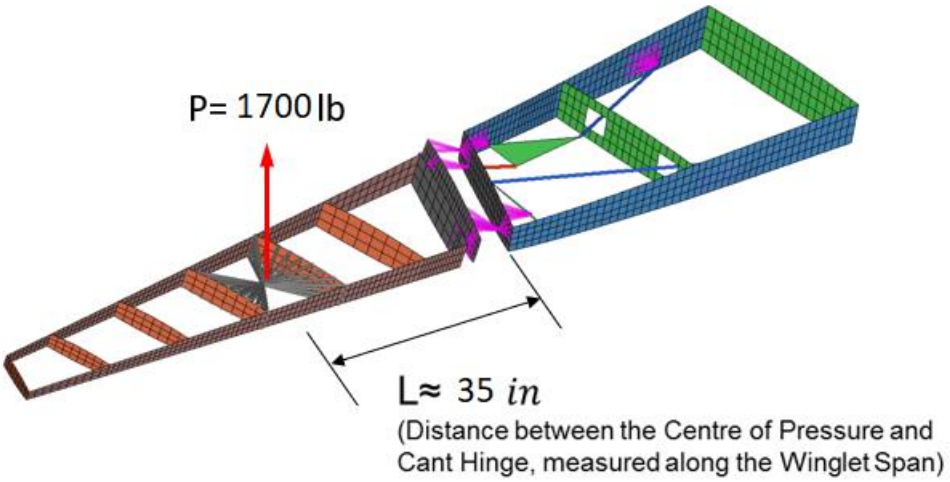

Figure 2.2: Load on morphlet [11].

Figure 2.2 can be used to calculate the hinge torque, T_H, required to change the cant angle of the morphlet:

$$T_H = P * L \tag{1}$$

in which P is the load and L is the distance between morphlet hinge and center of pressure. The hinge torque required is calculated to be 59500 lb-in, which is approximately equal to 6723 N*m.

Another design consideration is the volume of the wingbox in which the gearbox will be mounted.

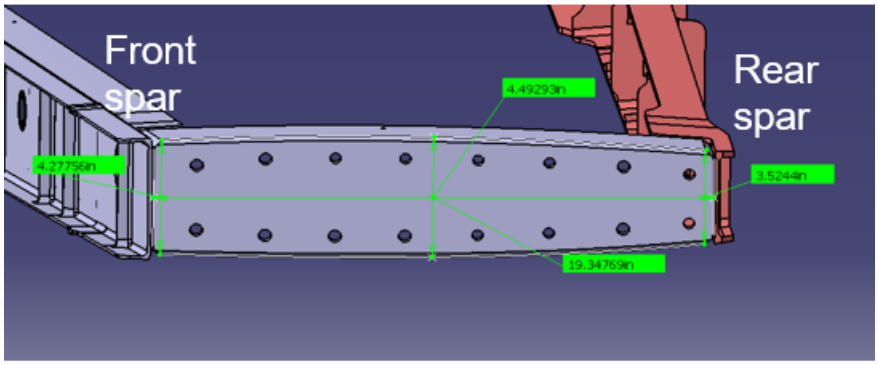

Figure 2.3: Dimensions of the wingbox [11].

Figure 2.3 shows the dimensions of the wingbox for which the gear drive will be designed. The allotted span-wise length is 50 inches, or approximately 1.27 meters.

2.2. Introduction to Proposed Designs

To achieve the cant angle motion of a morphlet two types of gear drives are considered: cycloidal and planetary gear drives. Both types of drives provide high reduction ratios within a relatively small volume. A cycloidal drive is a type of reduction drive that increases the output torque of a shaft input by taking advantage of the eccentric motion of a cycloidal gear.

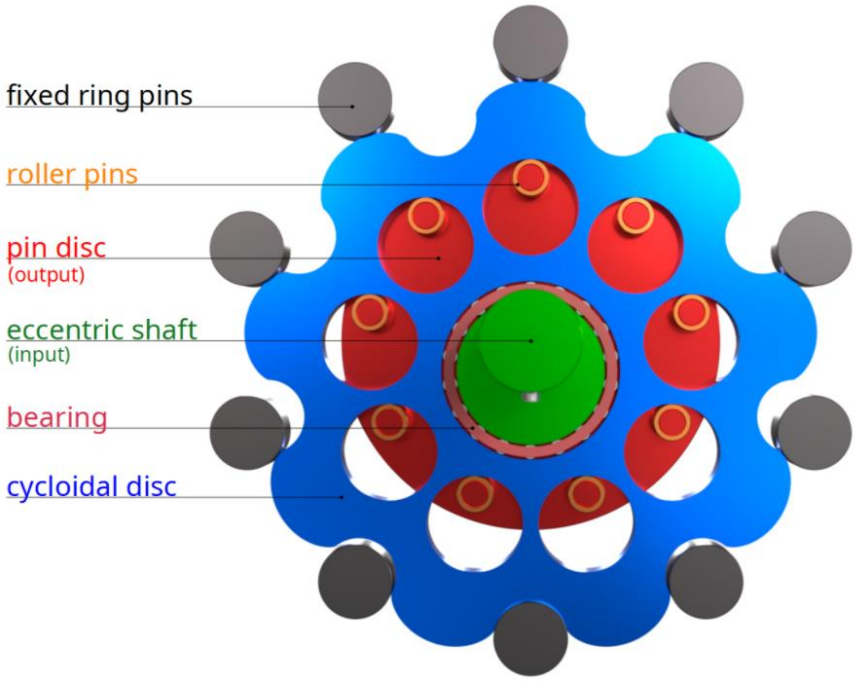

Figure 2.4: Labeled cycloidal gear diagram [12].

Figure 2.4 shows a simple cycloidal gear consisting of four main components. The cycloidal disk is the rotating and translating body of the cycloidal gear. Geometry of the cycloidal disk is formed by generating an epicycloid curve around a circle with the desired pith diameter. The cutting tool used to form the epicycloid curve (can be imagined as the thickness of the pencil tip used to draw the curve) will determine the exact shape of the disk and the size of the fixed ring pins. The cycloidal disk rolls on the inside of the fixed ring pins. The input of the cycloidal gear is the eccentric shaft; eccentric motion of the

shaft causes the rolling motion of the cycloidal disk inside of the fixed ring pin circle. Finally, the roller pins, also known as output pins, attached to the pin disk act as the output of the cycloidal gear. It is important to note that the output speed will be negative to that of the input speed (opposite direction). Detailed description of geometry formation for the cycloidal drive is discussed in Section 3. The design of the cycloidal drive for the electrically powered morphing winglet consists of one stepper motor, a bevel gearbox, and a two-stage cycloidal gearbox.

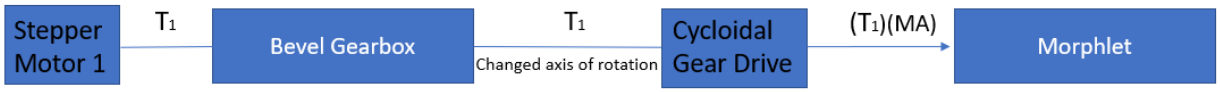

Figure 2.5: Power transmission diagram for cycloidal gear drive.

Figure 2.5 shows a power transmission diagram for the cycloidal gear drive. The reduction ratio of the bevel gearbox is 1:1 as it is only used to change the rotation axis of the system.

Planetary gear drives are another type of drive that offer high speed reduction ratios in a small volume while having an efficiency of approximately 97% [13]. In one stage, a planetary gear drive consists of a sun gear, a planet carrier or cage, and a ring gear.

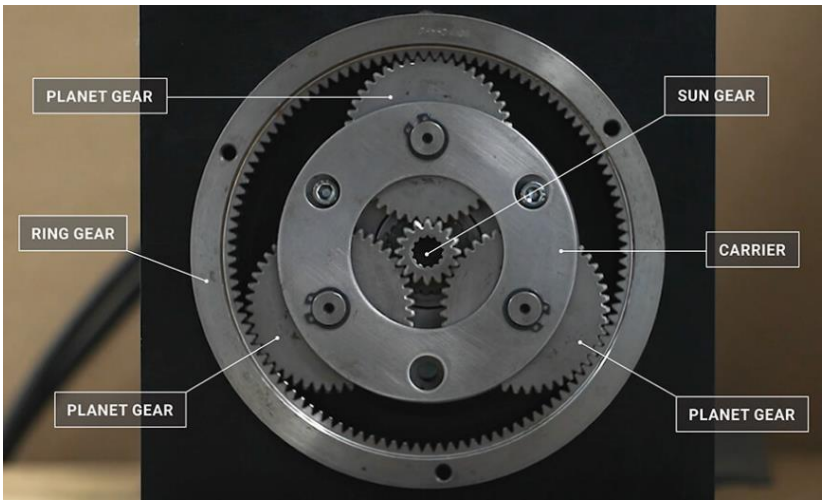

Figure 2.6: Labeled diagram of a planetary gear stage [13].

Figure 2.6 shows a labeled diagram of a stage in a planetary gear drive. In a planetary gear drive the sun gear, carrier, or the ring gear can act as power input or output. Fixing one of these components, for

example the ring gear, the other two components, the sun gear and carrier, act as power input or output. The speed reduction ratio depends on which component is fixed and which component acts as the input. Highest reduction ratio is achieved when the ring gear is fixed, and the sun gear is used as the input.

The design considered for the purposes of an electrically powered morphing winglet is a one stage differential planetary gear drive (DPGD) developed by Dr. Alexander Kapelevich of AKGears. The one stage DPGD consists of a regular planetary drive, however, two planets are compounded, and a single carrier holds the compounded planets. The ring gear of the second stage is free to rotate about the central axis and acts as the output of the DPGD. Since the planet carrier is not the output and does not transmit torque, it is referred to as a 'cage' for a one stage DPGD [14].

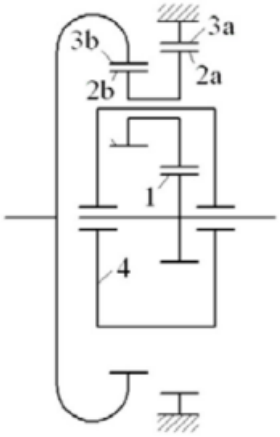

Figure 2.7: Compound planet one stage DPGD diagram [14].

Figure 2.7 shows a diagram of the one stage DPGD used for the design of the electrically powered morphing winglet. '1' is the input sun gear; '2a' is the planet gear meshing with the sun gear and '2b' is the compounded planet gear; '3a' is the ring gear for the planet gear that meshes with the sun gear; '3b' is the ring gear meshing with the compounded planet gear; '4' is the cage that holds the planets. In Figure 2.7 '3a' is the stationary ring and '3b' is the rotating ring which is used as the output.

A consideration for designing a planetary gear drive is which type of gear will be used. Three common types of gears are spur gears, helical gears, and herringbone gears. Spur gears are the most common types of gears used. They are easy to manufacture and only produce radial loads on shafts and

bearings. This allows for selecting smaller bearings and designing smaller shafts. Helical gears are often considered in place of spur gears because they offer a higher tooth contact ratio. This increases efficiency and lowers noise production. However, helical gears are hard to manufacture and produce both radial and axial loads on shafts and bearings. If helical gears are selected bearings need to be selected to handle both types of loads. Herringbone gears offer the same advantages as helical gears without producing axial loads on shafts and bearings. Herringbone gears, however, are very hard and costly to manufacture. Another drawback to using herringbone gears is that they cannot slide into mesh. This property of herringbone gears makes them impossible to use unless the ring gear of the planetary gear drive is manufactured in two pieces. Pictures of spur, helical and herringbone gears are provided in Figure 7.17, Figure 7.18, Figure 7.19 in Appendix C, respectively.

3. Cycloidal Gear Drive

The limited dimensions of the cross-sectional area of the wingbox limit the size of the cycloidal gear drive. Since the reduction ratio of the drive depends on the size of the cycloidal disk in each stage (assuming the minimum size of the cycloidal disk teeth is limited), the minimum size of the cycloidal drive is constrained by the required output torque. The minimum size of each individual component of the cycloidal drive is also constrained by the allowable stress of the selected materials of the components. For these reasons, the geometry sizing and material selection of key load-bearing components is done simultaneously. Finally, the engineering drawings of the input and output shafts of stage one and the eccentric cams of stage one and two are provided in Appendix A.

3.1. Geometry Sizing and Material Selection

CATIA V5 is used to model each component and create the final assembly. Static stress analysis is also performed on each component to help select a material that can bear the computed loads. Images and engineering drawings are provided in the appendix when noted.

3.1.1. Input Shaft

The input shaft is the input to the cycloidal gear. It interfaces with the shaft of the bevel gearbox output shaft and the eccentric cam. To link the input shaft of the cycloidal drive to the output shaft of the bevel gear, the output shaft of the bevel gear is designed as a coupler with a keyway. The input shaft of the cycloidal drive is inserted into the output shaft of the bevel gear and a key and a set screw is used to lock the two shafts together.

To link the input shaft to the eccentric cams, keyways are to be punched in the shaft and the cams and keys are to be used.

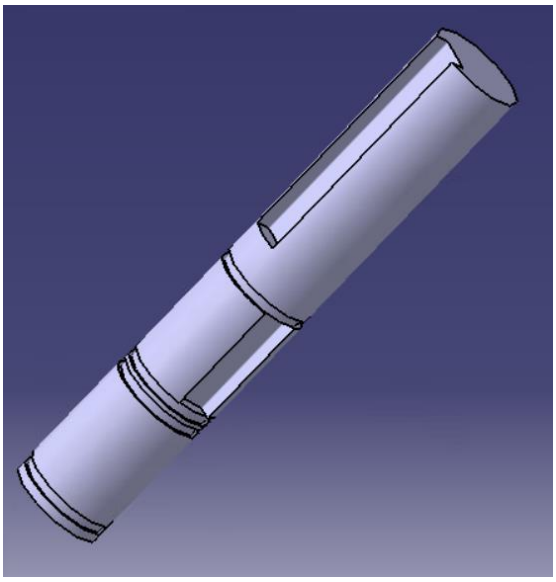

Figure 3.1: Keyways on cycloidal drive input shaft.

Figure 3.1 shows the keyways on the input shaft. The long keyway at the top of the shaft is to mate with the shaft coupler and link with the shaft of the stepper motor. The keyway in the middle of the shaft is to link the input shaft and the eccentric cam of the first cycloidal disk. A third keyway, not shown in Figure 3.1, is positioned 180 degrees offset to the keyway in the middle and mounts with the eccentric cam of the second cycloidal disk. Retaining ring notches are cut in the input shaft to hold the position of the eccentric cams of the cycloidal disk. The space between the eccentric cams (and the cycloidal disks) is 2.5 mm; this value is important as it is used to calculate the minimum output pin diameter. An engineering drawing of the input shaft is provided in Figure 7.2 in Appendix A.

Regular standards are used to size the keys and keyways and circlip notches on the input shaft.

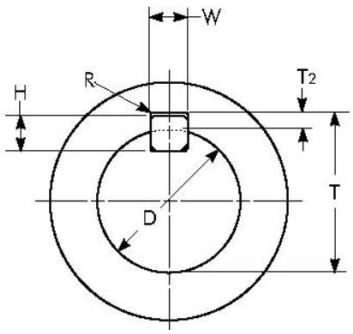

Figure 3.2: Keys and keyway sizing diagram [15].

Metric Key & Keyway Dimensions Per ISO/R773 – P9 Width Tolerance H										
Shaft Diameter		Key Size		Keyway Width			Keyway Depth		Keyway Radius	
"D"		Nominal		Hub "W"			Hub ""		"R"	
Over	Thru	Width "W"	Height "H"	Nominal	Min	Max	Min	Max	Min	Max
6	8	2	2	2	-.031	-.006	1.0	1.1	0.08	0.16
8	10	3	3	3	-.031	-.006	1.4	1.5	0.08	0.16
10	12	4	4	4	-.042	-.012	1.8	1.9	0.08	0.16
12	17	5	5	5	-.042	-.012	2.3	2.4	0.16	0.25
17	22	6	6	6	-.042	-.012	2.8	2.9	0.16	0.25
22	30	8	7	8	-.051	-.015	3.3	3.5	0.16	0.25
30	38	10	8	10	-.051	-.015	3.3	3.5	0.25	0.40
38	44	12	8	12	-.061	-.018	3.3	3.5	0.25	0.40
44	50	14	9	14	-.061	-.018	3.8	4.0	0.25	0.40

Figure 3.3: Keys and keyway sizing chart [15].

Figure 3.2 and Figure 3.3 are standard keys and keyway sizing diagram and chart based on the ISO/R773 standard. This diagram and chart are used to size all the keys and keyways on shafts and hubs unless noted otherwise. To size the notches for the retaining rings is based on the DIN 471 standard. An online calculator found at:

https://amesweb.info/Fasteners/Retaining-Ring/Circlips-External-Shafts-Metric.aspx

is used to size the notches for retaining rings.

To assign a preliminary material to the input shaft, as well as other components, the maximum stress subjected to the component needs to be known. To calculate the maximum stress finite element analysis (FEA) is performed on the input shaft using CATIA V5. Since the power flow for the cycloidal drive is unidirectional and the input loads on all components is known, it is possible to 'clamp' the output surfaces and apply the loads to input surfaces in CATIA V5. For the input shaft the input surface is the keyway linking the stepper motor the input shaft. The output surfaces are the two keyways that connect the input shaft to the eccentric cams. The input load is the 6 N*m torque delivered by the stepper motor.

Fillet radius is increased to a number greater than the size of the mesh to avoid stress singularities in CATIA V5. Results of the FEA stress analysis are shows in Appendix B.

Maximum stress subjected to the input shaft is calculated to be 671 MPa. Therefore, high yield steels must be used for the construction of the shaft. A potential material is 300m 4340 steel, which is a high yield steel commonly used in aircraft landing gears and airframe parts [16].

3.1.2. Eccentric Cam and Bearing

The eccentric cam is the component that mates with the input shaft and converts the centric motion of the input shaft to eccentric motion for the cycloidal disk. The eccentric motion of the cam allows the cycloidal disk to interact with the ring pins and rotate slower than the input shaft, providing the increase in torque. An important parameter relating to the design of the cycloidal disk is the eccentricity of the eccentric cam. Eccentricity is defined as the distance offset between the axis of rotation of the cycloidal disk and the axis of rotation of the input shaft.

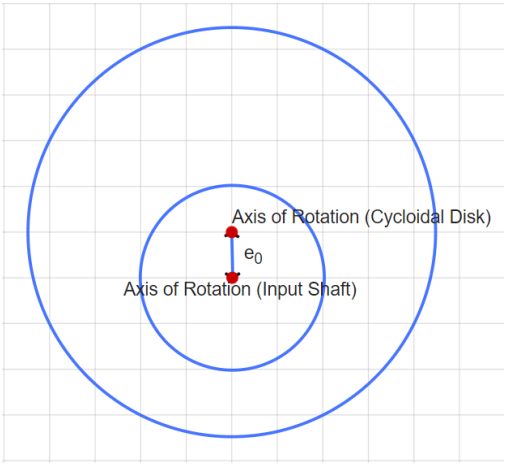

Figure 3.4: Eccentricity diagram.

Figure 3.4 gives a visual representation of eccentricity, where e_0 is the eccentricity measured in millimeters. The eccentricity of a cycloidal gear can be determined by selecting the module, defined as the ratio of the diameter of the pitch circle of the cycloidal gear, measured in millimeters, to the number of teeth on the cycloidal gear, and the coefficient of modification, which determined the difference

between an exact epicycloid and modified epicycloid. The value of the coefficient of modification is generally between 0.3 and 0.4 [17].

$$e_0 = \frac{m}{2}(1 - x) \tag{2}$$

Equation (2) is used to calculate the eccentricity, where m is the module and x is the coefficient of modification.

The diameter of the pitch circle of the cycloidal gear of stage one is selected to be 70 millimeters and the number of teeth of the cycloidal gear is selected to be 35.

$$m = \frac{d_1}{z_1}, d_1 = 70, z_1 = 35 \tag{3}$$

Using equation (3) the module, m, for stage one is calculated to be 2. The coefficient of modification is selected to be 0.3. The eccentricity of stage one of the cycloidal drive is calculated to be 0.7 millimeters. Similarly, for stage two of the cycloidal drive, the cycloidal gear pitch circle diameter is selected to be 93.5 millimeters and the number of teeth of the cycloidal gear is selected to be 34. Therefore, the calculated module of the cycloidal gear in stage two is 2.75. The coefficient of modification for the cycloidal gear in stage two is also selected to be 0.3. The eccentricity of stage two of the cycloidal drive is calculated to be 0.9625 millimeters. Engineering drawings and pictures of the eccentric cams of stage one and two are provided in Appendix A and Appendix C, respectively.

The maximum stress on the eccentric cam of stage one is calculated to be 363 MPa. For the eccentric cam of stage one lower yield steel can be used. A potential material is SCM435 structural steel. The maximum stress on the eccentric cam of stage two is calculated to be 906 MPa. 300m 4340 steel can also be used as the material for the eccentric cam of stage two. The bearing used between the eccentric cam of stage one and cycloidal disk of stage one is the K 16X22X12 needle roller and cage assemblies

bearing. The bearing used between the eccentric cam of stage two and cycloidal disk of stage two is a custom version of the PCM 252815 E bushings, for which the height of the bushing is changed from 15 millimeters to 10 millimeters. Both bearings are provided by skf.com.

3.1.3. Cycloidal Disk

Like a planet gear in a planetary gear drive, the cycloidal disk rotates around its axis of rotation as well as rolls inside of the circle created by the fixed ring pins. The combination of rotation and rolling motion is used to increase the torque of the input shaft. A hole is placed at the center of the cycloidal disk which is used to mount the eccentric cam and bearing. As shown in Figure 2.4 the cycloidal disk also contains holes used to link the output pins with the cycloidal disk.

To form the shape of the cycloidal disk the values of four key parameters need to be selected: module, coefficient of modification, number of teeth in the cycloidal disk and the coefficient of circle radius. Module and coefficient of modification parameters are the same as the ones introduced in earlier chapters. The number of teeth selected determines the total reduction ratio achieved by the stage. To calculate the reduction ratio the following equation is used:

$$\frac{1}{R.R} = \frac{1}{MA} = \frac{1}{z_1} \tag{4}$$

In which MA is the mechanical advantage and z_1 is the number of teeth on the cycloidal disk. The required mechanical advantage is selected based on the needs of the project and the restriction on the size of the gear drive. Using equation (4) and the required mechanical advantage, the number of teeth required on the cycloidal disk can be determined. The value of the coefficient of circle radius is typically 1 [17].

Once the values of the module, coefficient of modification and the number of teeth of the cycloidal disk are determined a parametric equation can be used to create a locus of points for the cycloidal disk. A spline is created through the points to create the geometry of the cycloidal disk.

$$X_w = \frac{m}{2}[(z_1 + 1)\sin(\varphi) - (1 - x)\sin\big((z_1 - 1)\varphi\big) + \frac{2[(1 - x)\sin((z_1 + 1)\,\varphi) - \sin(\varphi)}{\sqrt{1 - 2(1 - x)\cos(z_1 * \varphi) + (1 - x)^2}}] \quad (5)$$

$$Y_w = \frac{m}{2}[(z_1 + 1)\cos(\varphi) - (1 - x)\cos\big((z_1 - 1)\varphi\big) + \frac{2[(1 - x)\cos(z_1 + 1) - \cos(\varphi)}{\sqrt{1 - 2(1 - x)\cos(z_1 * \varphi) + (1 - x)^2}}] \quad (6)$$

Equation (5) and (6) are the parametric equations for the X and Y coordinates of the points used for the shape of the cycloidal disk, respectively. φ is the parameter measured in radians ranging from 0 to 2π.

To measure the initial thickness of the cycloidal disks an empirical equation from a thesis report from Linneaus University [17] is used:

$$B = 0.5 * r_2 \quad (7)$$

For which B is the disk thickness and r_2 is the radius of the pitch circle of the fixed ring pins. However, the final disk thickness is found by analysing the stress subjected to the cycloidal disk (in an iterative fashion). The first stage of the cycloidal drive will have a gear ratio (mechanical advantage) of 35:1 and a cycloidal disk thickness of 12 millimeters. The second stage of the cycloidal drive will have a gear ratio of 34:1 and a cycloidal disk thickness of 10 millimeters. Therefore, the cycloidal drive will provide a total mechanical advantage of 1190:1.

The diameter of the hole for the eccentric cam and bearing is determined by the outer diameter of the bearing selected. The diameter of the hole in the cycloidal disk for the eccentric cam and bearing in stage one is 22 millimeters. The diameter of the hole in the cycloidal disk for the eccentric cam and bearing in stage two is 28 millimeters.

To determine the diameter of the output pin holes the minimum value of the diameter of the output pins must be determined. This value is dependent upon the maximum bending stress subjected to the output pins and the material properties of the material selected for the output pins. The following set

of equations are acquired from a thesis report from Linneaus University and are used to calculate the minimum value of the output pins' diameter.

$$T_n = T_{in} * MA_n \tag{8}$$

Firstly, the output torque of the stage of the cycloidal drive needs to be determined. Equation (8) is used for this purpose, where T_n is the output torque of stage 'n', T_{in} is the input torque, and MA_n is the mechanical advantage of the stage. Next, the torque per cycloidal disk in each stage needs to be determined.

$$T_{g_n c_n} = \frac{T_n}{N} \tag{9}$$

The torque per cycloidal disk, $T_{g_n c_n}$, can be calculated using equation (9), where N is the number of cycloidal disks in the stage. To determine the maximum normal force, $F_{s,max}$, acting on one output pin the following equation is used.

$$F_{s,max} = \frac{4.8(T_{g_n c_n})}{z_w * r_{pin\ circle}} \tag{10}$$

It is assumed that each output pin shares an equal amount of load, therefore the maximum force is divided by z_w, the number of output pins for the stage, shown in equation (10). The radius of the pitch circle which the output pins are located on the cycloidal disk is designated by $r_{pin\ circle}$. To calculate the maximum bending stress the location along the length on the pin at which the maximum normal force acts must be determined.

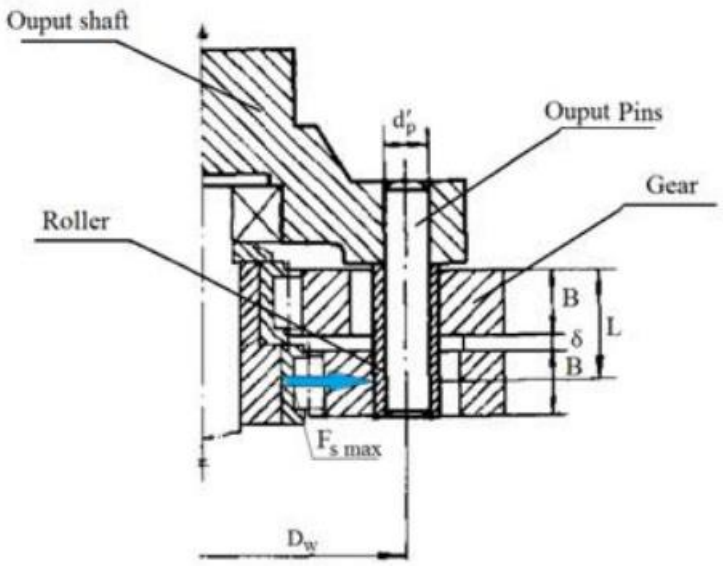

Figure 3.5: Labeled cross-section of cycloidal stage [17].

Figure 3.5 shows a labeled diagram of the cross-section of a stage in the cycloidal drive. For the calculations of the location at which the maximum normal force acts it is assumed to be the center of the first cycloidal disk; this is shown by the blue arrow in Figure 3.5.

$$L = 1.5B + \delta \tag{11}$$

$$L = 0.5B \tag{12}$$

Equation (11) represents Figure 3.5 in mathematical form for a stage containing two cycloidal disks (which is the case for the first stage). For a stage with one cycloidal disk (which is the case for the second stage) equation (12) is used. L is the location of maximum normal force along the output pin length, and δ is the distance between the cycloidal disks. For stage one δ is 2.5 millimeters. The cross-section constant of the output pins is used to calculate the maximum bending stress.

$$W = \frac{\pi * d_p^3}{32} \tag{13}$$

Equation (13) is used to calculate the cross-section constant, W, of the output pins. The variable d_p is the diameter of the output pins. The maximum bending stress acting on the output pins, $\sigma_{p,max}$, can be calculated by the following equation.

$$\sigma_{p,max} = \frac{F_{s,max} * L}{W} \tag{14}$$

The maximum allowable stress on the output pins is determined by the yield strength of the material used.

$$\frac{F_{s,max} * L}{W} = \sigma_{p,max} < \sigma_{yield} \tag{15}$$

The inequality shown in the equation (15), in which σ_{yield} is the yield strength of the material of the output pin, is used to determine the minimum pin diameter. Substituting equations (10), (11) or (12) depending on the number of cycloidal disks in the stage, (13) and (14) into equation (15) and simplifying for the output pin diameter the following inequality is obtained:

$$d_{p,min} > \sqrt[3]{\frac{4.8(T_{g_n c_n})(1.5B + \delta)(32)}{\pi(\sigma_{yield})(z_w)(r_{pin\ circle})}} \tag{16}$$

The inequality shown in equation (16) is used to select the material and determine the minimum diameter of the output pins. The sizing and material selection of the output pins is completed in a later section. Following the calculations of the minimum pin diameter of the output pins, a catalogue of bearings from SKF.com is used to select bearings for the output ring pins. The outer diameter of the selected bearings is used to calculate the diameter of the holes for the output pins in the cycloidal disks.

To account for the eccentric motion of the cycloidal disks the size of the holes for the output pins in the cycloidal disks must be adjusted.

$$d_{actual} = d_{outer\ diameter} + 2e_0 \tag{17}$$

Equation (17) gives the equation for the exact diameter, d_{actual}, required for the holes for the output pins in the cycloidal disk; $d_{outer\ diameter}$ is the outer diameter of the selected bearing.

The holes for the output pins' diameter on the cycloidal disk for stages one and two are calculated to be 14.4 millimeters and 21.925 millimeters, respectively.

FEA for a cycloidal gear is currently a novel topic. Theoretically half of the teeth on the cycloidal gear carry load [18]. However due to machining tolerances and other defects less than half of the lobes of the cycloidal disk will carry load. This makes stress analysis on the cycloidal disk and the fixed ring pins difficult. More time and resources are needed to perform accurate dynamic stress analysis on and select an appropriate material for the cycloidal disks. Conceptually, stainless steels or other low yield steels should be considered for the cycloidal disks of the first stage. High yield steels such as 300m steel or NC310YW steel should be considered for the cycloidal disk of the second stage.

3.1.4. Output Pins

Output Pins of a cycloidal drive revolve freely in the holes of the cycloidal disk and transfer the increased torque from the cycloidal disk to the output shaft. Therefore, the output pins must be able to withstand a high bending stress. The materials of the output pins for stage one and two are selected to be S960QL steel and NC310YW steel, respectively. Using the equations from section 3.1.2 and the bearing catalogue provided by SKF.com, the diameters of the output pins for stage one and two are selected to be 10 millimeters and 18 millimeters, respectively. The bearings selected for the output pins of stage one and two are K 10X13X10 TN needle roller and cage assemblies and PCM 182010 E bushings, respectively.

The output pins are mounted on a non-load-bearing plate using M2 screws for both stage one and stage two. The output shafts of both stages will be driven by loosely fitting the output pins in the base plate of the shafts. Pictures of the output pins of stage one and two are given in the appendix.

3.1.5. Output Shaft

The output shaft of a cycloidal gear allows the power transmission to continue to either the next stage of the cycloidal drive or to the load (which is the morphlet in this case). Therefore, the output shaft of stage one of the cycloidal drive will be the input shaft of stage two of the cycloidal drive. Bearings on the output pins allow the output shaft to rotate smooth about the central axis. Maximum stress on the output shaft is calculated to be 1540 MPa. A suitable material for the output shaft of stage one is NC310YW steel.

The output shaft of stage two will directly connect to the morphlet hinge. More analysis needs to be performed to select an appropriate mating style for the output shaft of stage two and the morphlet hinge. A key and keyway should be considered.

3.1.6. Housing

The housing of the cycloidal drive contains the fixed ring pins on which the cycloidal disk rolls. The parameters used to design the cycloidal gear disk are also used to design the housing. The number of fixed ring pins is always one greater than the number of teeth in the cycloidal disk, shown mathematically in the following equation:

$$z_2 = z_1 + 1 \tag{18}$$

In which z_2 is the number of fixed ring pins. To calculate the diameter of the pitch circle on which h the fixed ring pins are located the following equation is used:

$$d_2 = \frac{m * z_2}{2} \tag{19}$$

In which d_2 is the diameter of the pitch circle of fixed ring pin center location. The diameter of the fixed ring pins is calculated by using the following equation:

$$d_c = 2m \tag{20}$$

In which d_c is the diameter of the pin.

The diameter of the pitch circle of fixed ring pin location for stage one and two are calculated to be 72 millimeters and 96.25 millimeters, respectively. The diameter of fixed ring pins for stage one and two are calculated to be 4 millimeters and 5.5 millimeters, respectively. To complete the housing, the fixed ring pins are integrated inside a cylinder which has an inner diameter equal to that of the fixed ring pins' pitch circle. The housings for stage one and two are combined to form one housing for the cycloidal drive.

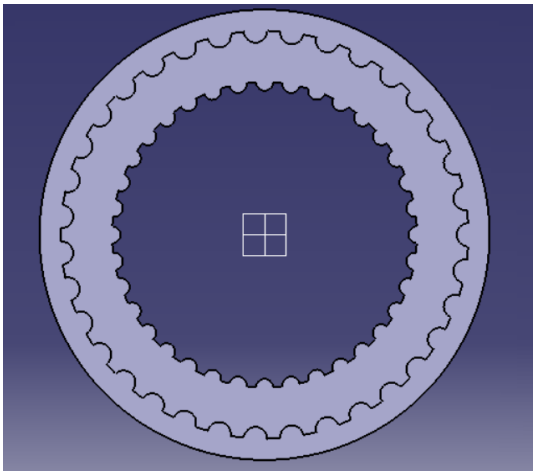

Figure 3.6: Top view of cycloidal drive housing.

Figure 3.6 shows the top view of the cycloidal drive housing. The fixed ring pins are integrated with the housing to increase structural rigidity and save space. An isometric view of the housing can be found in the appendix. The material used to manufacture the housing of the cycloidal drive depends on the dynamic analysis of the stage two cycloidal disk. Cycloidal disk of stage two and the cycloidal drive

housing should be manufactured from the same material. Isometric view of the housing is provided in the appendix.

3.2. Bevel Gearbox

The bevel gearbox of the cycloidal drive is used to change the axis of rotation of the system. The input shaft interfaces with the output shaft of the stepper motor. To link the input shaft of the bevel gearbox to the output shaft of the stepper motor a custom shaft coupler is required. (This is because the shaft of the stepper motor is manufactured using English units whereas the input shaft of the cycloidal drive is designed using metric units). Stafford Collars, Couplings & Unique Components is a shaft couplings manufacturer that offer custom shaft couplings. A quote can be filled out at:

https://shaft-collars-couplings.staffordmfg.com/item/metric-rigid-shaft-couplings/customizable-steel-clamp-couplings/15873

including the part style, bore and keyway sizes to manufacture a shaft coupling for the shaft of the stepper motor and the input shaft of the cycloidal drive.

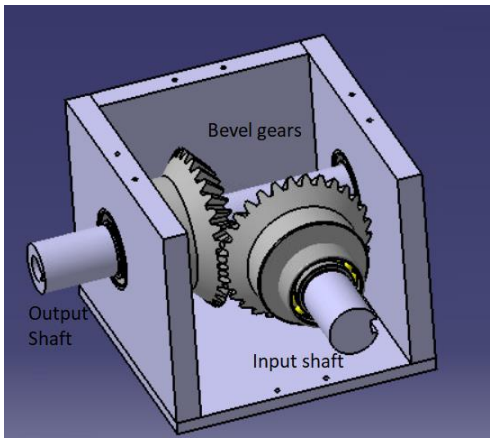

Figure 3.7: Labeled bevel gearbox.

Figure 3.7 shows a labeled diagram of the bevel gearbox. The bevel gears are selected from an online catalogue at:

https://khkgears2.net/catalog6/

The bevel gears selected are SMA2-30 bevel gears. These gears are selected based on their size, bore diameter and torque rating. W 63804-2RS1 deep groove ball bearings are used to allow free rotation and support the input and output shafts.

3.3. Assembly Inside Wingbox

The cycloidal drive is designed to fit inside the wingbox cross-section shown in Figure 2.3, however the exact methods of mounting the components inside the wingbox are not established.

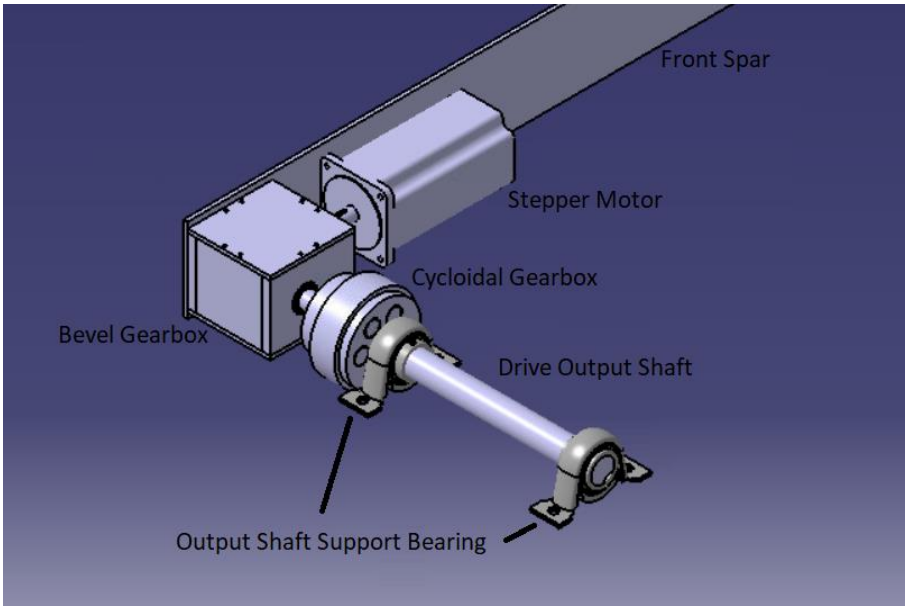

Figure 3.8: Labeled diagram of cycloidal drive assembly in wingbox.

Figure 3.8 shows a labeled diagram of the cycloidal drive inside the wingbox. The drive output shaft and the output shaft support bearings can be designed based on the coupling method used for the winglet. For this stage in the design the drive output shaft has a diameter of 30 millimeters and the support bearings are selected to be P 30 TR pillow block ball bearing units provided by skf.com. More pictures of the complete cycloidal assembly are provided in Appendix C.

4. Planetary Gear Drive

Planetary gear drives are like cycloidal gear drives in regard to their operation. Both have a ring in which gears, one in the case of cycloidal drive and two or more in the case of planetary drives, roll. However, unlike a cycloidal drive, planetary drives use standard spur gears as the load carrying components. This increases the manufacturability of the gears in a planetary drive and lowers components' costs. Analysis of spur gears is also easier than that of cycloidal gears because of the large amounts of empirical data and better simplified models of available. In contrast to cycloidal drives, in which the load carrying capacity increases as the diameters of the output pins and cycloidal disk increase, the load carrying capacity of a planetary drive increases as the face width of the teeth on the gears increases. This is desirable for the purposes of the electrically powered morphing winglet because the spanwise and chord-wise length of the wingbox is much larger than the thickness of the wingbox. Furthermore, typically, planetary gear drives perform at higher efficiencies than planetary gear drives [18]. For these reasons, a planetary gear drive may be a better option to power the electrically powered morphing winglet.

Mechanical advantage provided by the DPGD is given by the following equation, taken from a report by Dr. Kapelevich [14]:

$$u = \frac{1 + \frac{z_{3a}}{z_{sun}}}{1 - \frac{z_{2b} z_{3a}}{z_{2a} z_{3b}}} \tag{21}$$

In which, u is the gear ratio, z_{sun} is the number of teeth on the sun gear, z_{2a} is the number of teeth of the planet gear that meshes with the stationary ring gear, z_{2b} is the number of teeth of the planet gear that meshes with the rotating ring gear, z_{3a} is the number of teeth on the stationary ring gear, and z_{3b} is the number of teeth of the rotating ring gear.

For the design of the DPGD, four parameters must be selected: the module of the sun gear m_{sun}, number of teeth of the sun gear, number of teeth of the stationary ring gear and the number of planets in the DPGD N_p. The following equations are used to determine the rest of the parameters in equation (21) [19]:

$$z_{2a} = (z_{3a} - z_{sun})/2 \tag{22}$$

$$z_{2b} = z_{2a} \tag{23}$$

$$z_{3b} = z_{3a} + N_p \tag{24}$$

$$m_{2b} = \frac{z_{3a} - z_{2a}}{m_{sun}(z_{3b} - z_{2b})} \tag{25}$$

The following conditions must be met for the DPGD to behave correctly [19]:

- Number of teeth of sun gear must be divisible by the number of planets.
- Number of teeth of all gears must be whole.
- Number of teeth of the stationary ring gear must be divisible by the number of planets.
- All planets must fit around sun gear without overlap.

The DPGD is designed using equations (21) to (25) and the conditions given above.

4.1. Geometry Sizing and Material Selection

To design the gear tooth profile of each gear a parametric method is used. Four parameters are used to design the overall geometry of the gears. These parameters are module, pressure angle, number of teeth and face width.

The module and number of teeth are used to determine the radius of pitch circle, radius of addendum circle, radius of base circle and radius of dedendum circle using the following equations.

$$R_p = m * z/2 \tag{26}$$

In which R_p is the radius of pitch circle, m is the module and z is the number of teeth.

$$R_a = R_p + m \tag{27}$$

In which R_a is the radius of addendum circle.

$$R_b = R_p - 0.5 * m \tag{28}$$

In which R_b is the radius of base circle.

$$R_d = R_b - m \tag{29}$$

In which R_d is the radius of dedendum circle. The pressure angle is used to create the exact geometry of the tooth profile. Finally, the face width is used as the pad length in CATIA V5.

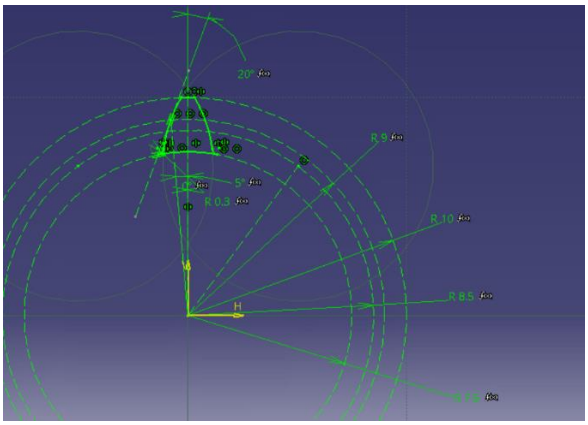

Figure 4.1: Diagram of sun gear tooth profile.

Figure 4.1 shows a diagram of the gear tooth profile of the sun gear. The constrained circles are the pitch circle, addendum circle, base circle and pitch circle. The 20 degrees angle is the pressure angle.

4.1.1. Input Shaft and Sun Gear

The sun gear is the gear at the center of the planetary gear drive that meshes with the planet gears and mates with the input shaft. For this design, the input shaft and the sun gear are meant to be manufactured as one piece. This lowers the internal stresses in the sun gear. The module and number of teeth of the sun gear is selected to be 1 millimeter and 18, respectively. The module of the planets that mesh with the stationary ring gear and the stationary ring gear is also 1 millimeter.

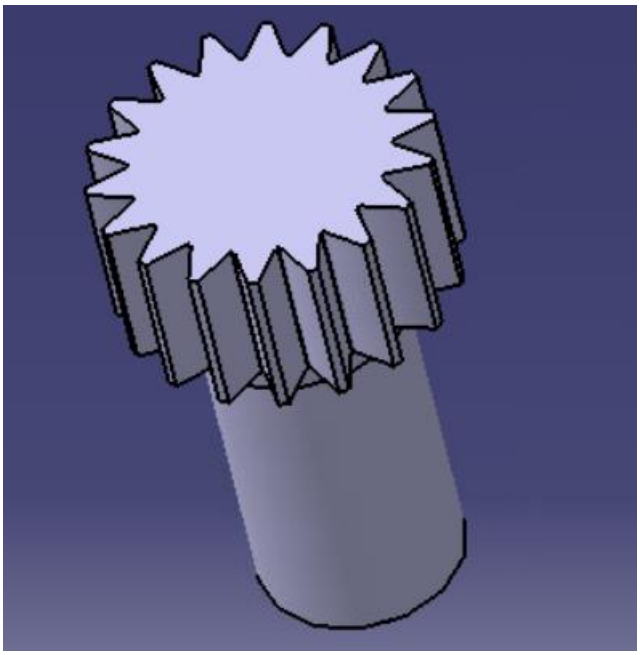

Figure 4.2: Input shaft and sun gear.

Figure 4.2 shows an isometric view of the sun gear and input shaft.

The maximum stress subject to the sun gear is 54 MPa, a potential material for the sun gear is 6061 aluminum. The bearing selected to support the input shaft is the W 61701 deep groove ball bearing.

4.1.2. Planet Gears

The stage one planet gear meshes with the sun gear and the stationary ring gear. Number of teeth of the planet gear of stage one is calculated to be 36. The stage two planet gear meshes with the rotating ring gear. Number of teeth of the planet gear of stage two is calculated to be 36. The module of the planets in stage two is selected to be 0.9474 millimeters; this will also be the module of the rotating ring gear. In a DPGD the planets of stage one and two are joined together. A cage is used to hold the planets in place and a bearing is used to allow the planets to rotate around their rotation axis freely. The bearing used for the cage is K 22X26X10 needle roller and cage assemblies.

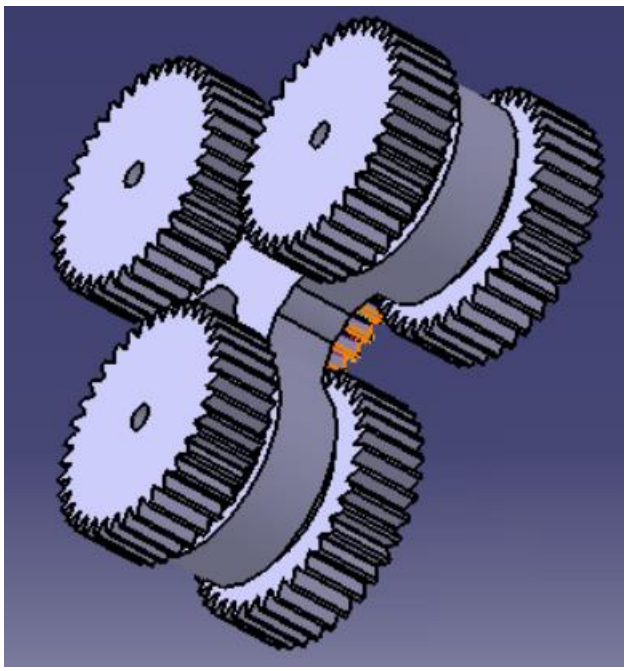

Figure 4.3: Cage assembly.

Figure 4.3 shows the assembly of the planets of stage one and two and the cage. The maximum stress subject to the planets of stage one is 34 MPa, a potential material is 6061 aluminum. The maximum stress subject to the planets in stage two is 674 MPa, a potential material is SCM440 steel. Pictures of the stage one and stage two planet gears are provided in the appendix.

4.1.3. Ring Gear

The stationary ring gear meshes with the planet gears of stage one and the rotating ring gear meshes with the planets of stage two. The stationary ring gear is integrated with the housing to save space inside the wingbox. On the other hand, the rotating ring gear is connected to the output shaft by M2 screws. The number of teeth of the stationary and rotating ring gears is 90 and 93, respectively. The maximum stress calculated on the stationary ring gear is 22 MPa, a potential material is 6061 aluminum. The maximum stress calculated on the rotating ring gear is 568 MPa, a potential material is SCM440 steel.

4.2. Future Considerations

The total gear ratio provided by the designed planetary gear drive is 180:1, based on equation (21). Future considerations for the design of a planetary gear drive for application in an electrically powered morphing winglet include increasing the output torque of the drive to meet the requirements of the load of the morphlet. However, designing spur gears to withstand the tooth bending forces applied by the morphlet whilst still being small enough to fit inside the wingbox is difficult with current manufacturing methods. This can be shown by using an online spur gear calculator provided by KHKGears.com.

Allowable circumferential force (N)	7118.73767	7118.73767
Allowable torque (N• m)	355.93688	355.93688
Allowable power (kW)	3.72736	3.72736
Normal module	5	
Normal pressure angle	20° 0' 0"	
Helix angle	0° 0' 0"	
	Small gear	Large gear
Number of teeth	20	20

Figure 4.4 Allowable torque calculated by KHKGears for spur gear pair [20].

Figure 4.4 shows the allowable torque for a spur gear with a diameter of 100 millimeters (approximately maximum allowable diameter for gear to fit in wingbox) and a material tensile strength of 980 MPa [21]. The maximum allowable input torque for one spur gear is 356 N*m. If torque is equally distributed among three planet gears the maximum allowable torque is 1068 N*m. This is still significantly lower

than the required output torque. The only way to significantly increase the allowable torque for a spur gear is to increase the tooth thickness. This, however, means increasing the module, which leads to larger gears and lower efficiencies. According to calculations of KHKGears, a spur gear, manufactured from high tensile strength material, small enough to fit inside the gearbox cannot tolerate loads from the morphing winglet.

5. Conclusions

Actuation of an electrically powered morphing winglet using a stepper motor given the constraints of the wingbox is plausible. To increase the torque of a motor to the required torque at the morphlet hinge a cycloidal gear drive and a planetary gear drive are considered.

The two types of motors considered are the stepper motor and the servo motor. Servo motors offer very precise angular position and velocity control but provide relatively low torque. Stepper motors sacrifice some of the precise control offered by servo motors, however, stepper motors provide high torque and are less expensive when compared to servo motors. Therefore, for the purposes of this project, a stepper motor is selected to acuate the electrically powered morphing winglet.

The cycloidal drive consists of a HT34-487 stepper motor, a bevel gearbox, and a cycloidal gearbox. The HT34-487 stepper motor is selected based on having the highest torque available whilst still abiding by the constraints of the gearbox. The bevel gearbox consists of two meshing bevel gears with equal number of teeth, bearings, and the gearbox housing. The bevel gears selected are SMA2-30 bevel gears. The SMA2-30 bevel gears are selected based on being able to fit inside of the wingbox, having an allowable torque equal to the output torque of the HT34-487 stepper motor, and having a bore diameter to mate with a designed shaft.

The cycloidal gearbox consists of two stages of cycloidal gears. The first stage of the cycloidal gear box provides a gear ratio of 35:1 and the second stage provides a gear ratio of 34:1. Therefore, the total gear ratio provided by the cycloidal gearbox is 1190:1. This provides sufficient speed reduction to allow the selected stepper motor to actuate the morphlet. Initial material selection is performed on some of the major components of the cycloidal gearbox. The initial materials selected for the input shaft is 300m 4340 steel. The initial material selected for the eccentric cams of stage one and two are SCM435 structural steel and 300m 4340 steel, respectively. The initial materials selected for the output pins of stage one and two are S960QL steel and NC310YW steel, respectively. The initial material selected for the output shaft of

stage one is NC310YW steel. FEA simulations on these components is performed to ensure the maximum stress subjected to the components does not exceed the yield strength of the materials selected. The figures of this analysis are provided in Appendix B.

A differential planetary gear drive is also considered for the actuation of the electrically powered morphing winglet. Parametric methods are used to design the sun, planet, and ring gears in CATIA V5. The sun gear is designed to have a module of 1 millimeter and 18 teeth. The planet gears of stage one are designed to have a module of 1 millimeter and 36 teeth. The planet gears of stage two are designed to have a module of 0.9474 millimeters and 36 teeth. The stationary ring gear is designed to have 90 teeth and the rotating ring gear is designed to have 93 teeth. The designed differential planetary gear drive provides a gear ratio of 180:1. Therefore an extra stage or gearbox is needed to allow the HT34-487 stepper motor to actuate the morphlet.

However, according to calculations performed using an online gear tooth bending calculator it is unfeasible to design spur gears (which are used in the planetary gear drive) that can handle the torque required to actuate the morphlet while still fitting inside the wingbox.

5.1. Future Work

To consider the cycloidal drive a viable option for the actuation of the electrically powered morphing winglet future work one simulation needs to be performed. Dynamic modeling of the cycloidal disk and the housing must be done to ensure that the selected materials are able to withstand the subjected stresses. Force analysis on the bearings should also be considered and bearing selection should be iterated based on the findings. Finally, system simulation or empirical testing should be performed on the system to understand the fatigue behaviour of the components and their selected materials. The simulation will also provide insight on the vibrational nature of the cycloidal disks.

6. References

[1] B. Dunbar, "NASA - NASA Dryden Technology Facts - Winglets," 2008. [Online]. Available: https://www.nasa.gov/centers/dryden/about/Organizations/Technology/Facts/TF-2004-15-DFRC.htm. [Accessed February 2021].

[2] NASA, Artist, *Wing Tip Vortex | How Things Fly.*. [Art]. NASA Langley Research Center, 2020.

[3] B. Co, "Aircraft with movable winglets and method of control". United States of America Patent US8651431B1, 9 August 2011.

[4] F. Xi, A. Moosavian, G. Campos, U. Choudhuri, C. Sun and R. Buchkazanian, "ANALYSIS AND CONTROL OF AN ACTUATION-REDUNDANT PARALLEL MECHANISM REQUIRING SYNCHRONIZATION," Ryerson University, Toronto, 2019.

[5] D. Smith, R. Ajaj, A. Isikveren and M. Friswell, "Multi-Objective Optimization for the Multiphase Design of Actice Polymorphing Wings," *Journal of Aircrafts,* no. 49, pp. 1153-1160, 2012.

[6] C. Gonzalez, "What's the Difference Between Pneumatic, Hydraulic, and Electrical Actuators?," [Online]. Available: https://www.machinedesign.com/mechanical-motion-systems/linear-motion/article/21832047/whats-the-difference-between-pneumatic-hydraulic-and-electrical-actuators. [Accessed February 2021].

[7] TiMOTION Technology, "Advantages and Drawbacks of Pneumatic, Hydraulic, and Electric Linear Actuators," TiMOTION Technology, 2017. [Online]. Available: https://www.timotion.com/it/news/news_content/blog-articles/general/advantages-and-drawbacks-of-pneumatic,-hydraulic,-and-electric-linear-actuators?upcls=1481266229&guid=1499762723. [Accessed February 2021].

[8] "Servo Motors," 2020. [Online]. Available: https://www.engineering.com/ProductShowcase/ServoMotors.aspx. [Accessed February 2021].

[9] "Stepper Motors," 2020. [Online]. Available: https://www.engineering.com/ProductShowcase/StepperMotors.aspx. [Accessed February 2021].

[10] Applied Motion Products, "HT34-487 - NEMA 34 High Torque Step Motor," [Online]. Available: https://www.applied-motion.com/products/stepper-motors/ht34-487. [Accessed February 2021].

[11] *Electro-Design,* Ryerson University, 2020.

[12] tec-science, "How does a cycloidal drive work?," tec-science, 14 January 2019. [Online]. Available: https://www.tec-science.com/mechanical-power-transmission/planetary-gear/how-does-a-cycloidal-gear-drive-work/. [Accessed February 2021].

[13] LANCEREAL, "Planetary Gears: Principles Of Operation," LANCEREAL, 29 November 2019. [Online]. Available: https://www.lancereal.com/planetary-gears-principles-of-operation/. [Accessed March 2021].

[14] A. Kapelevich, "High Gear Ratio Epicyclic Drives Analysis," GEARTECHNOLOGY, 2014.

[15] Engineers Edge, "Standard Metric Keys Keyways for MEtric Bores with One Key," Engineers Edge, [Online]. Available: https://www.engineersedge.com/hardware/standard_metric_keys_keyways_13449.htm. [Accessed Februuary 2021].

[16] TW METALS, "300M ALLOY STEEL (4340M)," TW METALS, [Online]. Available: https://www.twmetals.com/products/bars/alloy-bar/300m.html. [Accessed February 2021].

[17] B. Borislavov, I. Borisov and V. Panchev, "Design of a Planetary-Cyclo-Drive Speed Reduced Cycloid Stage, Geometry, Element Analysis," Linneus University, Växjö, 2012.

[18] S. Mraz, "Comparing Cycloidal and Planetary Gearboxes," MachineDesign, 3 February 2011. [Online]. Available: https://www.machinedesign.com/news/article/21829580/comparing-cycloidal-and-planetary-gearboxes. [Accessed March 2021].

[19] D. Hartkop, Director, *Split Ring Compound Planet Epicyclic Gear.* [Film]. David Hartkop, 2017.

[20] KHKGears, *Spur • helical gear Calculation of bending strength,* KHKGears, 2021.

[21] JFS Steel, "SNCM420," JFS Steel, [Online]. Available: https://www.jfs-steel.com/en/product/SNCM420.html#:~:text=SNCM420%20is%20a%20kind%20of,resistance%20and%20contact%20fatigue%20strength.. [Accessed March 2021].

[22] AmesWeb, *EXTERNAL CIRCLIP DIMENSIONS FOR SHAFTS (METRIC - DIN 471),* AmesWeb.

[23] Stafford Manufacturing Corp. | The Super Source for Collars & Couplings, *CUSTOMIZABLE STEEL CLAMP COUPLINGS,* Boston: Stafford Manufacturing Corp. | The Super Source for Collars & Couplings.

[24] STEEL GRADES, "SCM435," STEEL GRADES, [Online]. Available: https://www.steel-grades.com/Steel-Grades/Structure-Steel/SCM435.html. [Accessed March 2021].

[25] Aubert & Duval, "Through hardening steels," Aubert & Duval, [Online]. Available: https://www.aubertduval.com/alloy/721/. [Accessed March 2021].

[26] Masteel, "S960QL," Masteel, [Online]. Available: https://masteel.co.uk/s960ql/. [Accessed March 2021].

[27] C. Cavallo, "All About 6061 Aluminum (Properties, Strength and Uses)," thomasnet, [Online]. Available: https://www.thomasnet.com/articles/metals-metal-products/6061-aluminum/. [Accessed March 2021].

[28] Ju Feng Special Steel Co., Ltd., "SCM440," Ju Feng Special Steel Co., Ltd., [Online]. Available: https://www.jfs-steel.com/en/product/SCM440.html. [Accessed March 2021].

[29] SKF, "K 16X22X12," SKF, [Online]. Available: https://www.skf.com/ca/en/products/rolling-bearings/roller-bearings/needle-roller-bearings/needle-roller-and-cage-assemblies/productid-K%2016X22X12. [Accessed March 2021].

[30] SKF, "PCM 252815 E," SKF, [Online]. Available: https://www.skf.com/ca/en/products/plain-bearings/bushings-thrust-washers-strips/bushings/productid-PCM%20252815%20E. [Accessed March 2021].

[31] SKF, "K 10X13X10 TN," SKF, [Online]. Available: https://www.skf.com/ca/en/products/rolling-bearings/roller-bearings/needle-roller-bearings/needle-roller-and-cage-assemblies/productid-K%2010X13X10%20TN. [Accessed March 2021].

[32] SKF, "PCM 182010 E," SKF, [Online]. Available: https://www.skf.com/ca/en/products/plain-bearings/bushings-thrust-washers-strips/bushings/productid-PCM%20182010%20E. [Accessed March 2021].

[33] SKF, "W 63804-2RS1," SKF, [Online]. Available: https://www.skf.com/ca/en/products/rolling-bearings/ball-bearings/deep-groove-ball-bearings/productid-W%2063804-2RS1. [Accessed March 2021].

[34] SKF, "P 30 TR," SKF, [Online]. Available: https://www.skf.com/ca/en/products/mounted-bearings/ball-bearing-units/pillow-block-ball-bearing-units/productid-P%2030%20TR. [Accessed March 2021].

[35] SKF, "W 61701," SKF, [Online]. Available: https://www.skf.com/ca/en/products/rolling-bearings/ball-bearings/deep-groove-ball-bearings/productid-W%2061701. [Accessed March 2021].

[36] SKF, "K 22X26X10," SKF, [Online]. Available: https://www.skf.com/ca/en/products/rolling-bearings/roller-bearings/needle-roller-bearings/needle-roller-and-cage-assemblies/productid-K%2022X26X10. [Accessed March 2021].

[37] C. Wang, H. H. Khodaparast and M. I. Friswell, "Conceptual study of a morphing winglet based on unsymmetrical stiffness," *Aerospace Science and Technology,* vol. 58, pp. 546-558, 2016.

7. Appendices

7.1. Appendix A: Data Figures and Tables

Table 7.1: Stage 1 eccentric cam bearing data [29].

Name	K 16X22X12
Link	https://www.skf.com/ca/en/products/rolling-bearings/roller-bearings/needle-roller-bearings/needle-roller-and-cage-assemblies/productid-K%2016X22X12
Bearing Type	Needle roller and cage
Dynamic Load Rating	11 kN
Static Load Rating	12.5 kN
Inner Diameter	16 mm
Outer Diameter	22 mm
Length	12 mm

Table 7.2: Stage 2 eccentric cam bearing data [30].

Name	PCM 252815 E
Link	https://www.skf.com/ca/en/products/plain-bearings/bushings-thrust-washers-strips/bushings/productid-PCM%20252815%20E
Bearing Type	Bushings
Dynamic Load Rating	28.5 kN
Static Load Rating	88 kN
Inner Diameter	25 mm
Outer Diameter	28 mm
Length	15 mm

Table 7.3: Stage 1 output pins bearing data [31].

Name	K 10X13X10 TN
Link	https://www.skf.com/ca/en/products/rolling-bearings/roller-bearings/needle-roller-bearings/needle-roller-and-cage-assemblies/productid-K%2010X13X10%20TN
Bearing Type	Needle roller and cage
Dynamic Load Rating	4.57 kN
Static Load Rating	5.7 kN
Inner Diameter	10 mm
Outer Diameter	13 mm
Length	10 mm

Table 7.4: Stage 2 output pins bearing data [32].

Name	PCM 182010 E
Link	https://www.skf.com/ca/en/products/plain-bearings/bushings-thrust-washers-strips/bushings/productid-PCM%20182010%20E
Bearing Type	Bushings
Dynamic Load Rating	14 kN
Static Load Rating	43 kN
Inner Diameter	18 mm
Outer Diameter	20 mm
Length	10 mm

Table 7.5: Bevel gear bearing data [33].

Name	W 63804-2RS1
Link	https://www.skf.com/ca/en/products/rolling-bearings/ball-bearings/deep-groove-ball-bearings/productid-W%2063804-2RS1
Bearing Type	Deep groove ball bearings
Dynamic Load Rating	3.12 kN
Static Load Rating	2.08 kN
Inner Diameter	20 mm
Outer Diameter	32 mm
Length	10 mm

Table 7.6: Cycloidal drive output shaft bearing data [34].

Name	P 30 TR
Link	https://www.skf.com/ca/en/products/mounted-bearings/ball-bearing-units/pillow-block-ball-bearing-units/productid-P%2030%20TR
Bearing Type	Pillow block ball bearing units
Dynamic Load Rating	19.5 kN
Static Load Rating	11.2 kN
Inner Diameter	30 mm
Outer Diameter	39.7 mm
Length	38 mm

Table 7.7: Sun gear bearing data [35].

Name	W 61701
Link	https://www.skf.com/ca/en/products/rolling-bearings/ball-bearings/deep-groove-ball-bearings/productid-W%2061701
Bearing Type	Deep groove ball bearings
Dynamic Load Rating	0.527 kN
Static Load Rating	0.265 kN
Inner Diameter	12 mm
Outer Diameter	18 mm
Length	4 mm

Table 7.8: Cage bearing data [36].

Name	K 22X26X10
Link	https://www.skf.com/ca/en/products/rolling-bearings/roller-bearings/needle-roller-bearings/needle-roller-and-cage-assemblies/productid-K%2022X26X10
Bearing Type	Needle roller and cage
Dynamic Load Rating	8.8 kN
Static Load Rating	13.7 kN
Inner Diameter	22 mm
Outer Diameter	16 mm
Length	10 mm

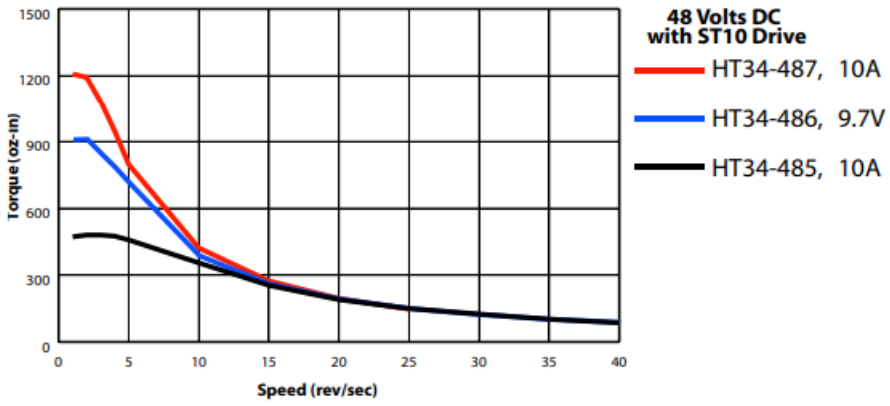

Figure 7.1: Torque - speed curve of HT34-487 motor [10].

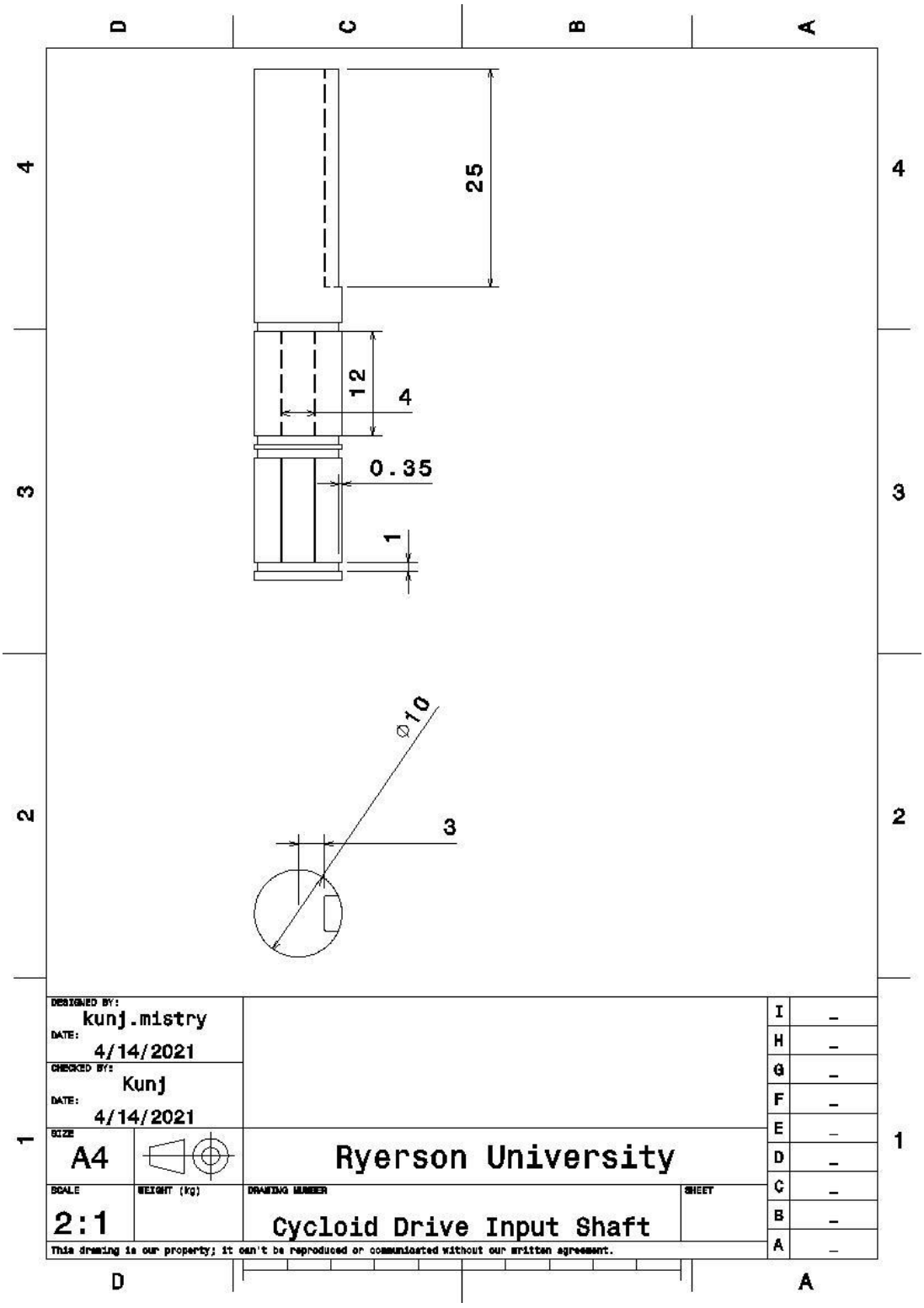

Figure 7.2: Cycloid drive input shaft drawing.

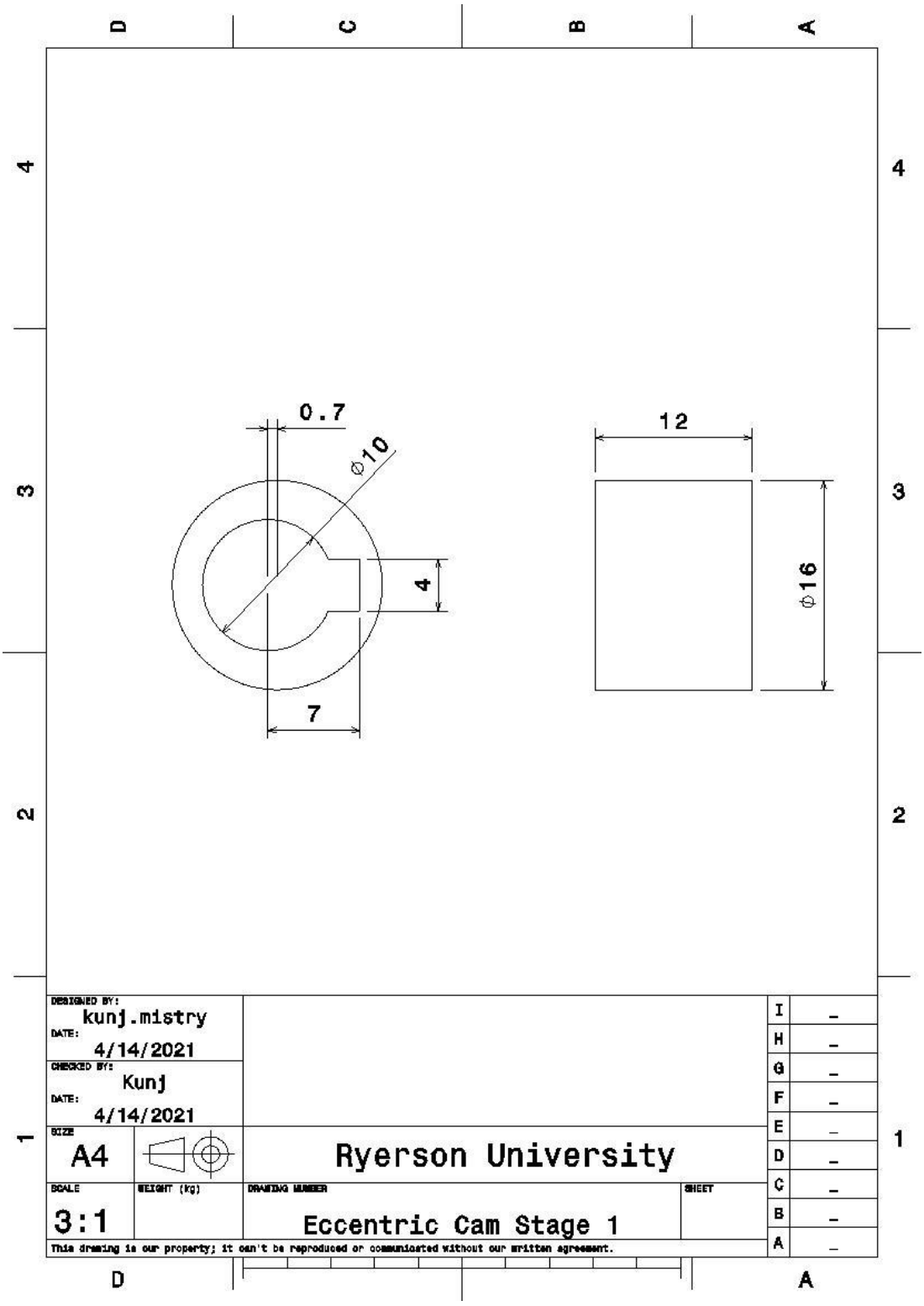

Figure 7.3: Eccentric cam stage 1 engineering drawing.

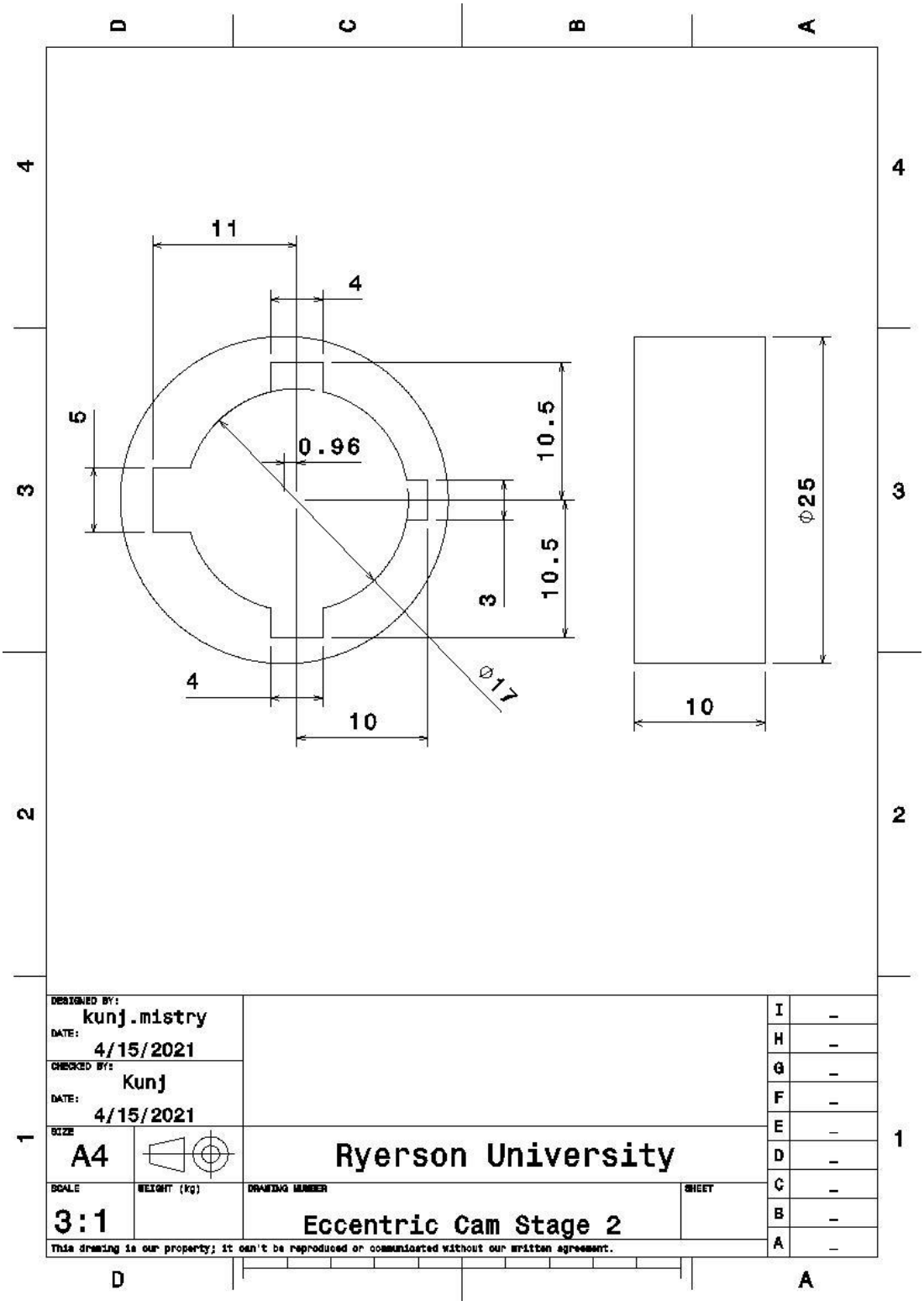

Figure 7.4: Eccentric cam stage 2 engineering drawing.

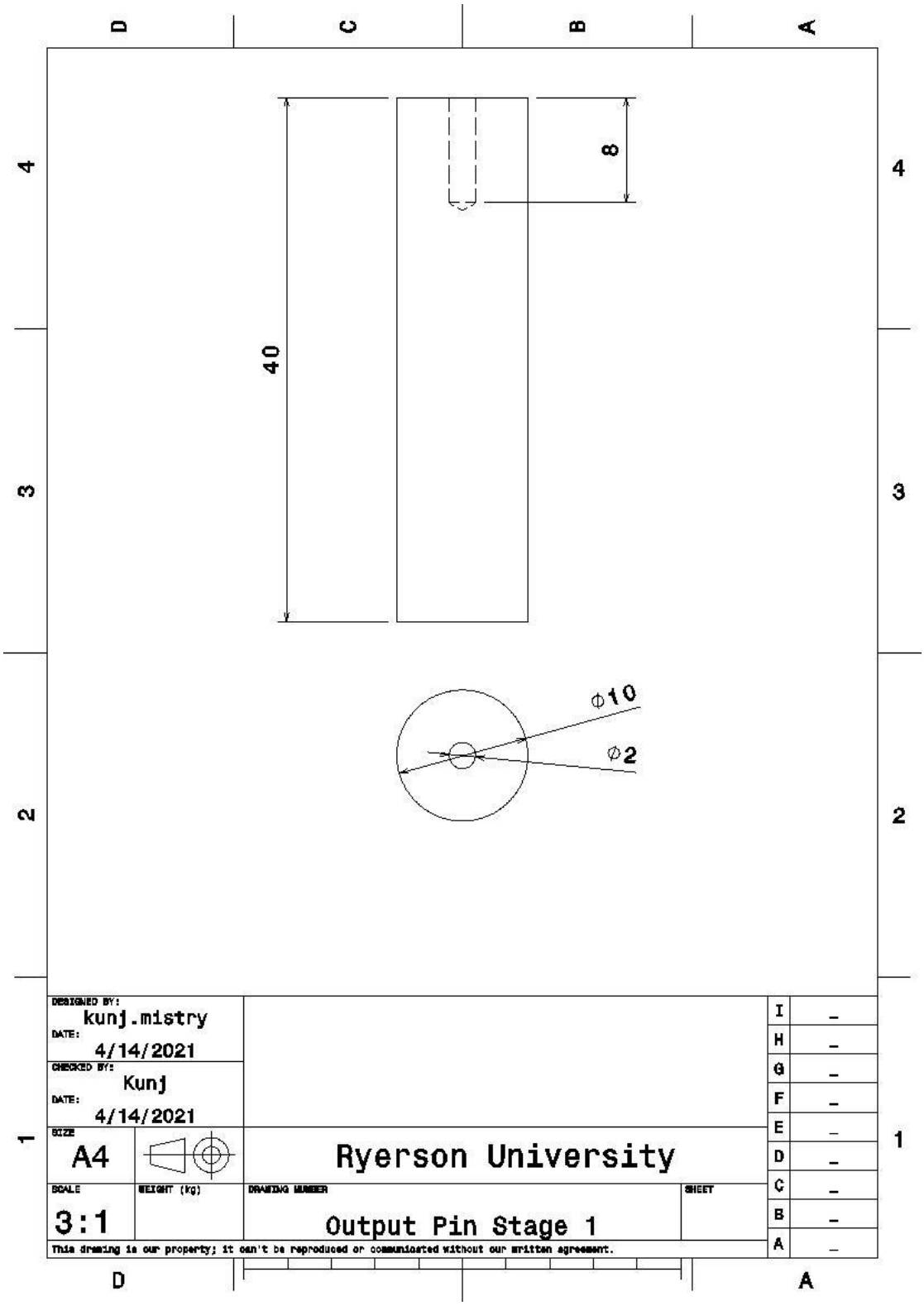

Figure 7.5: Output pins stage 1 engineering drawing.

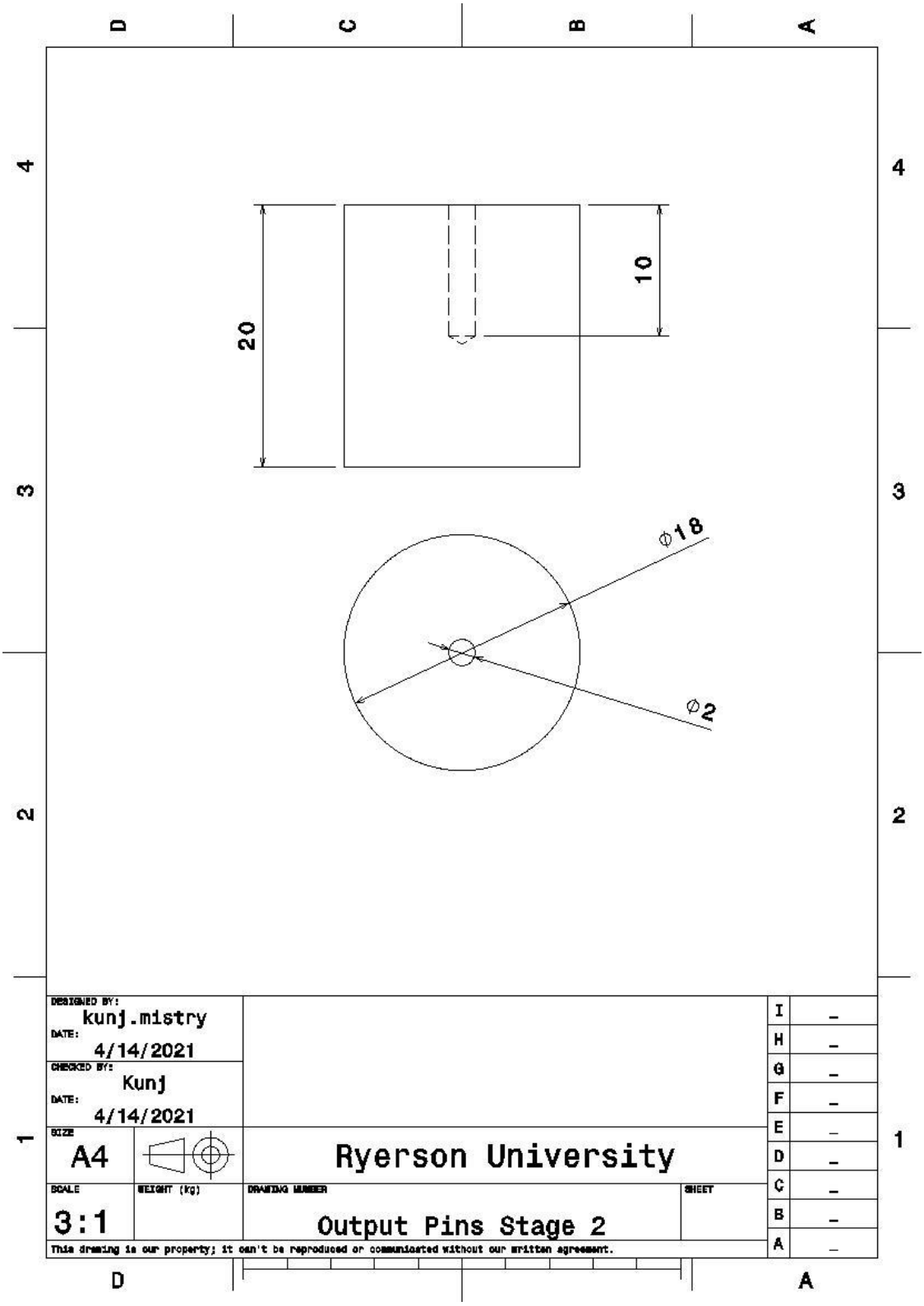

Figure 7.6: Output pins stage 2 engineering drawing.

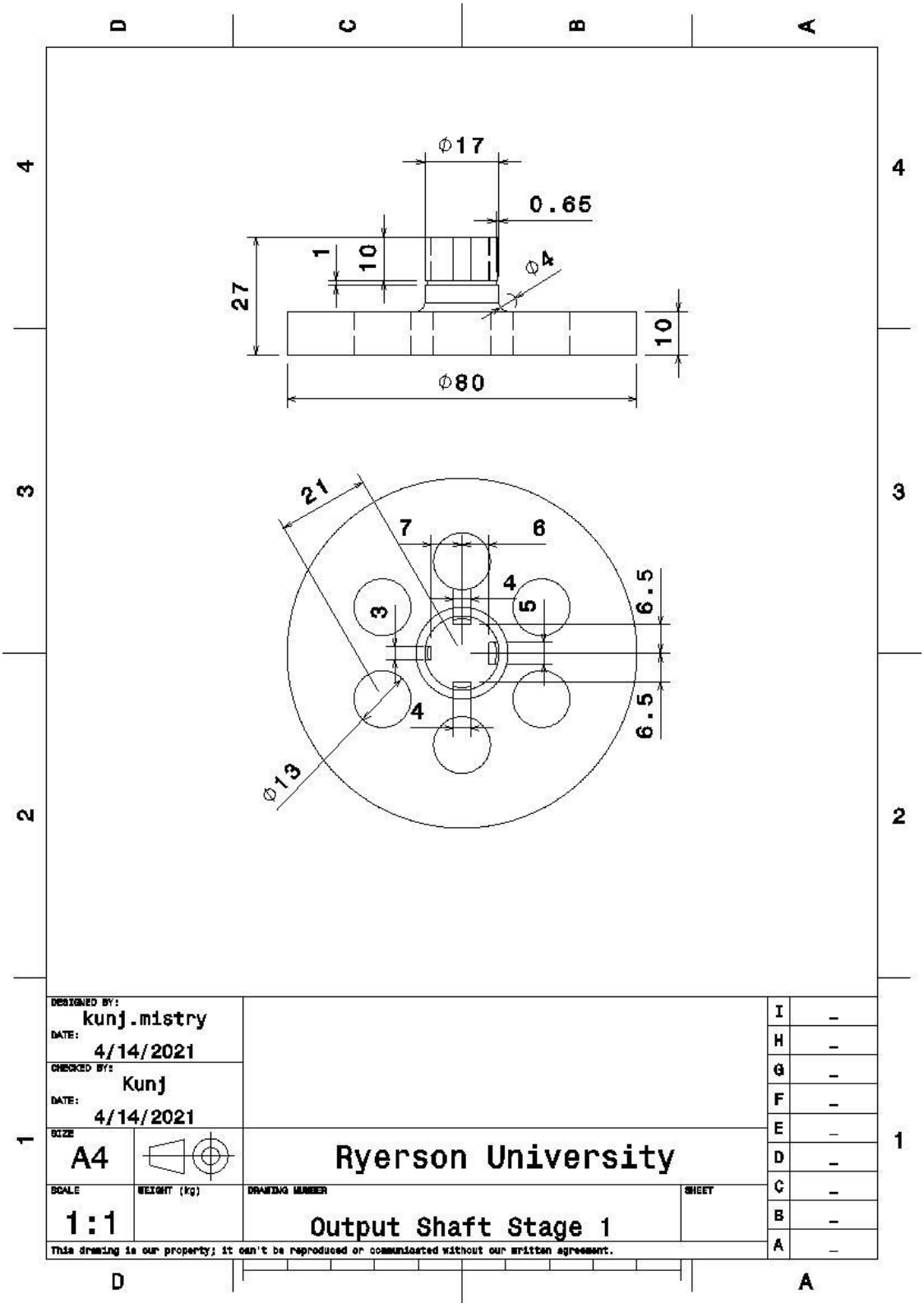

Figure 7.7: Output shaft stage 1 engineering drawing.

7.2. Appendix B: Static Stress Analysis

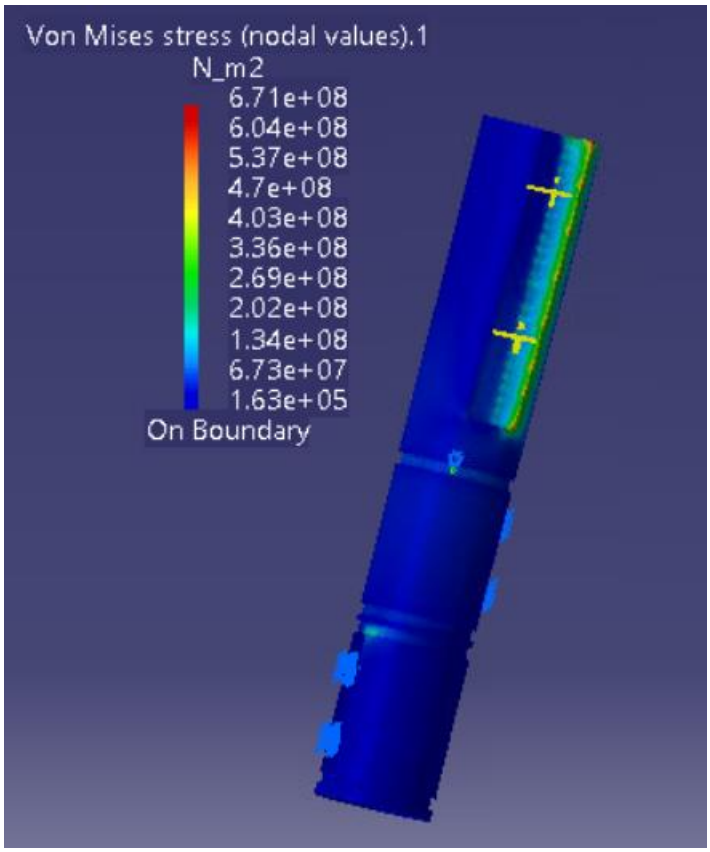

Figure 7.8: Input shaft stress analysis.

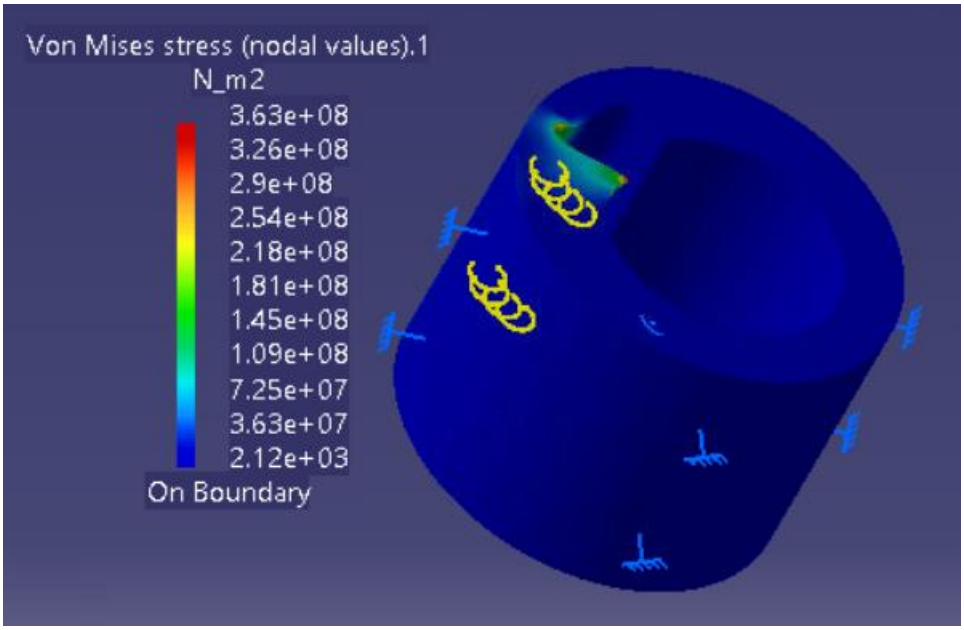

Figure 7.9: Eccentric cam stage 1 stress analysis.

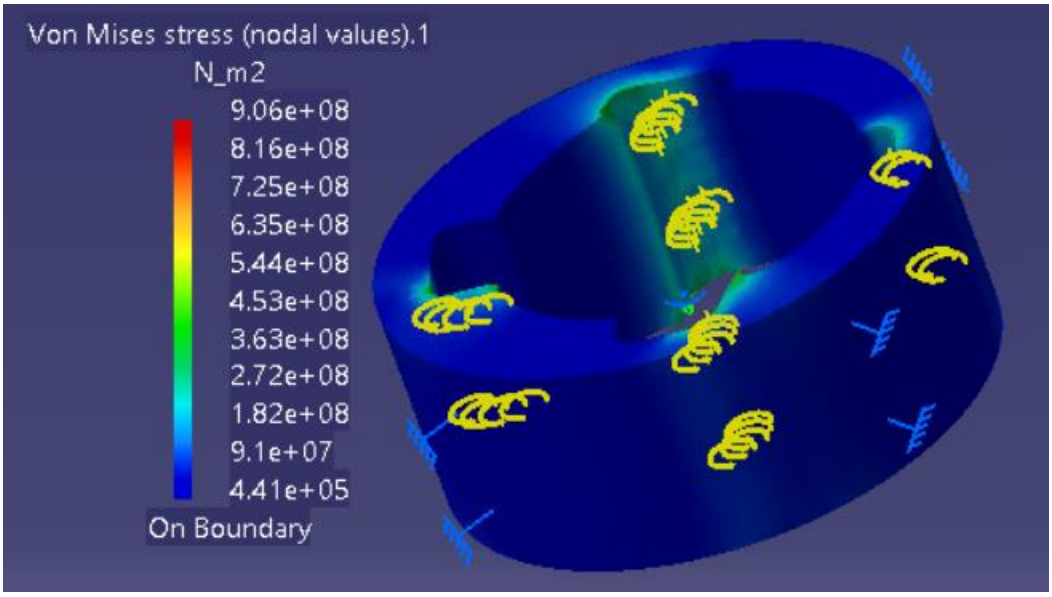

Figure 7.10: Eccentric cam stage 2 stress analysis.

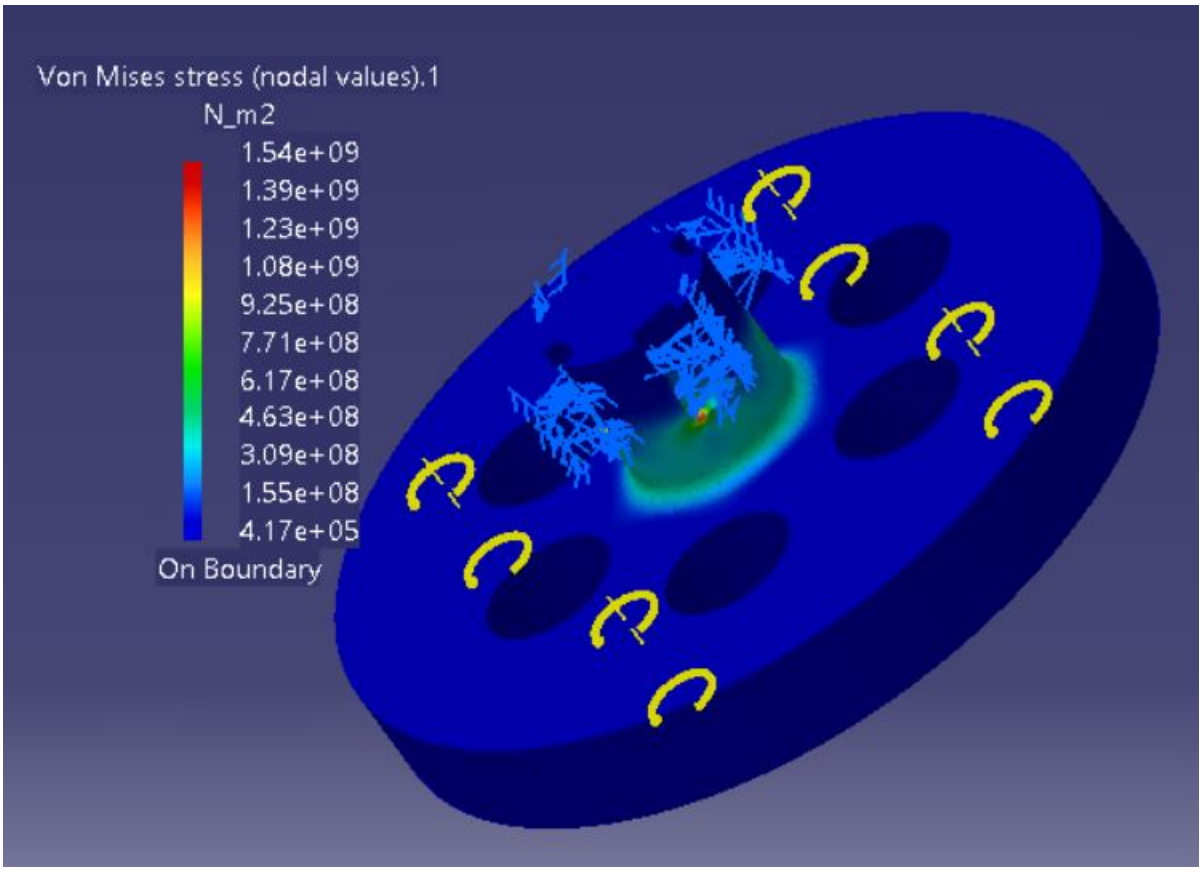

Figure 7.11: Output shaft stage 1 stress analysis.

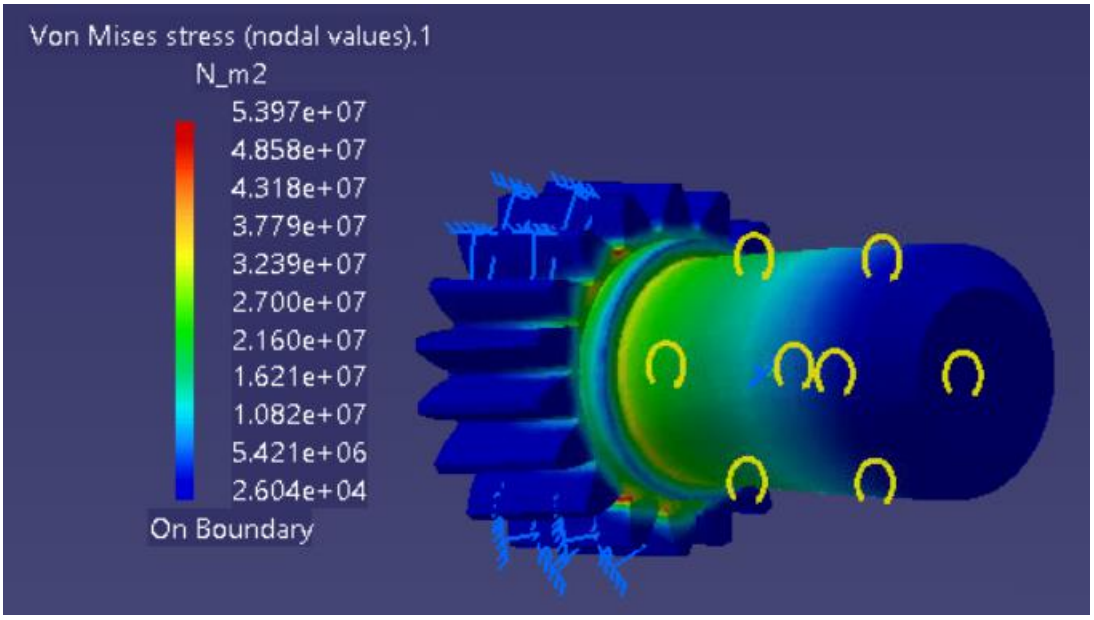

Figure 7.12: Sun gear and input shaft stress analysis.

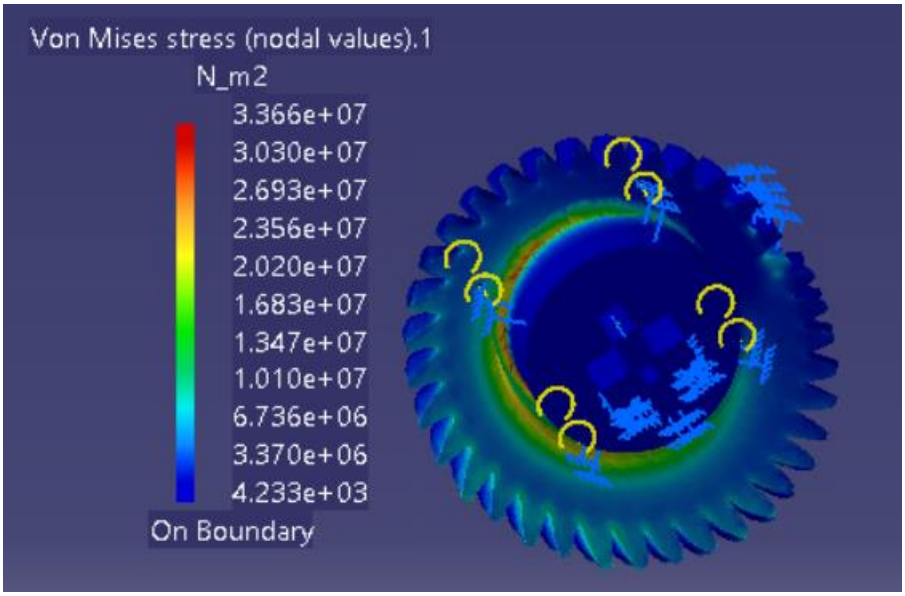

Figure 7.13: Stage 1 planet gear stress analysis

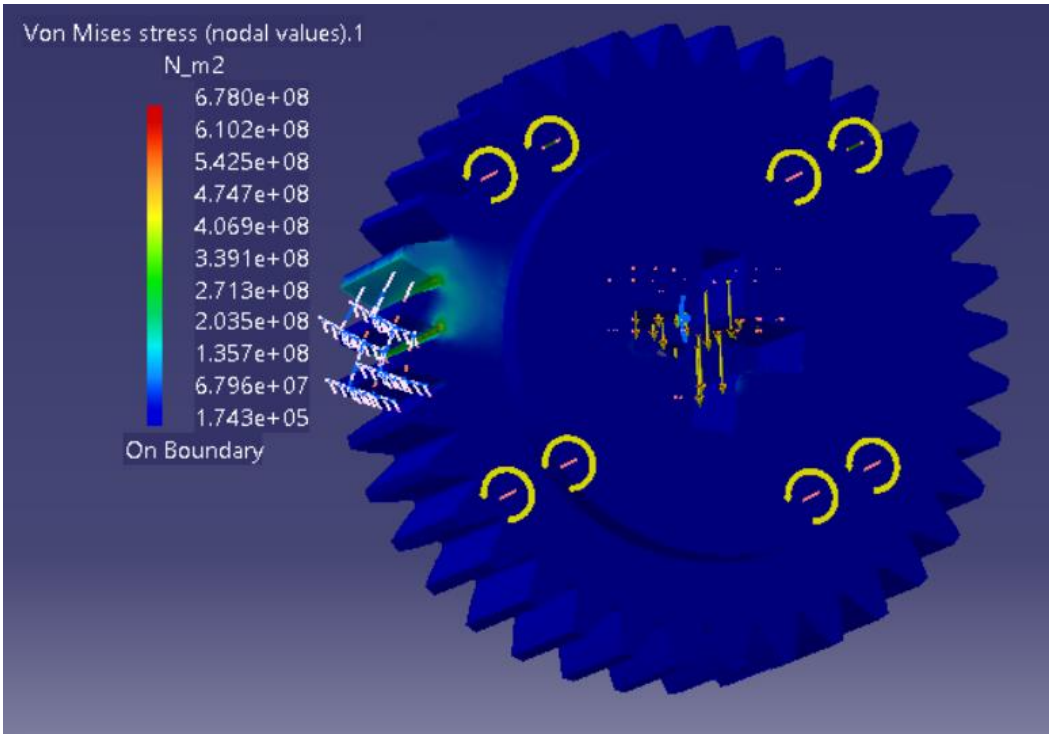

Figure 7.14: Stage 2 planet gear stress analysis.

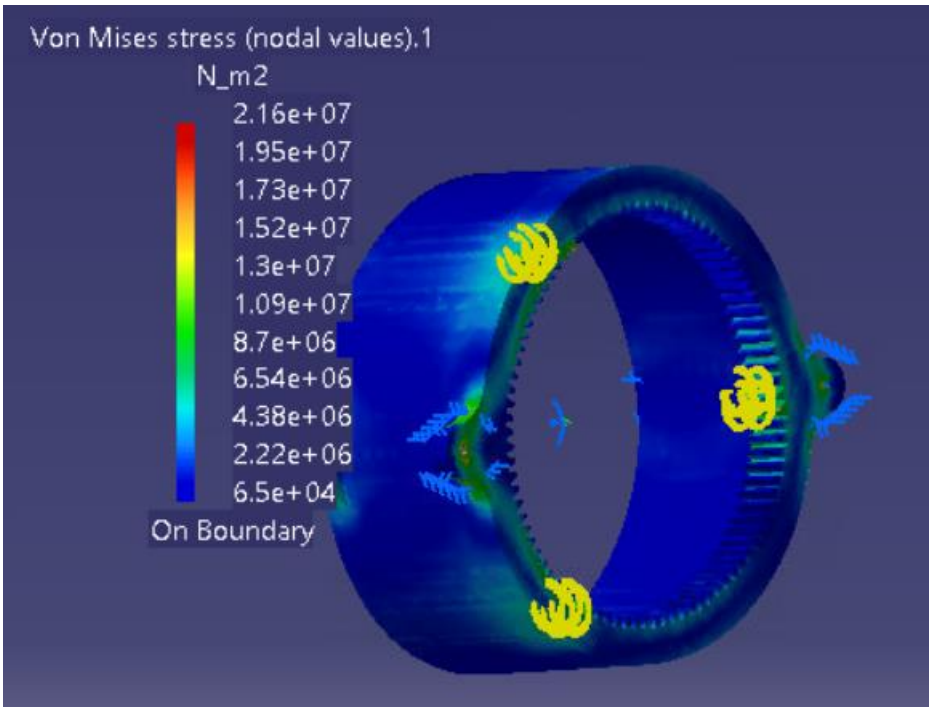

Figure 7.15: Stationary ring gear stress analysis.

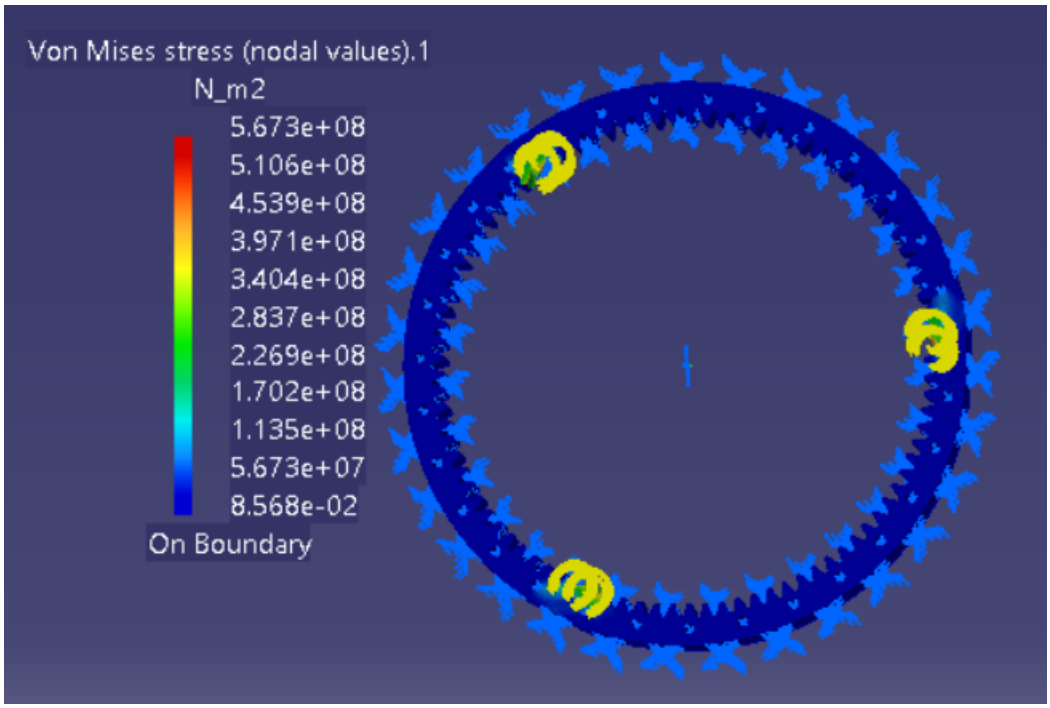

Figure 7.16: Rotating ring gear stress analysis.

.

7.3. Appendix C: Components' and Assembly Images

Figure 7.17: Spur gear [15].

Figure 7.18: Helical Gear [15].

Figure 7.19: Herringbone Gear [15].

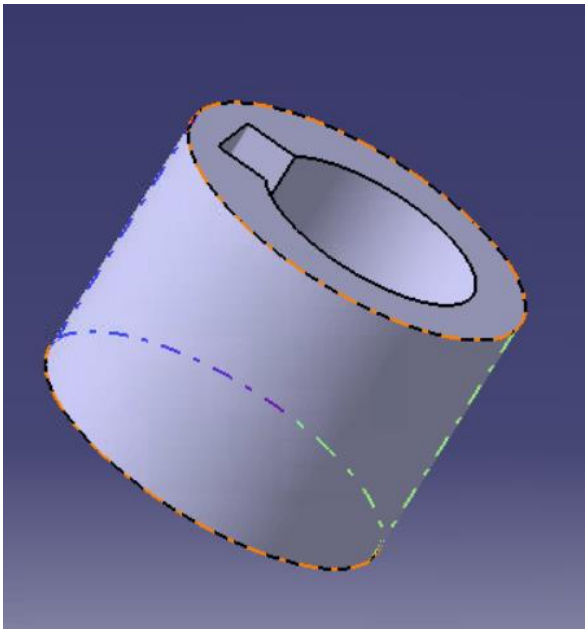

Figure 7.20: Eccentric cam stage 1.

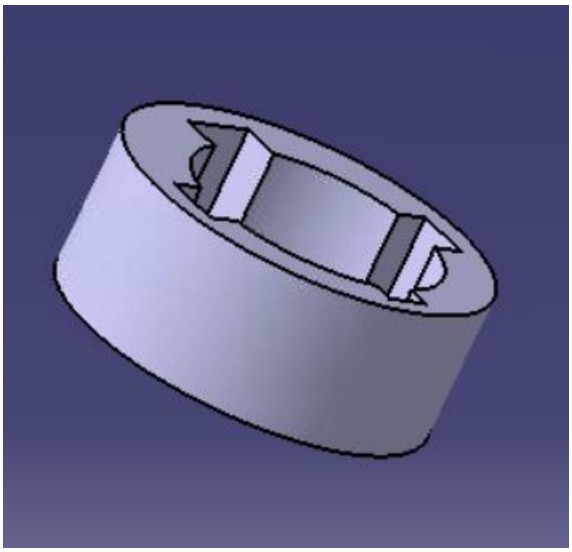

Figure 7.21: Eccentric cam stage 2.

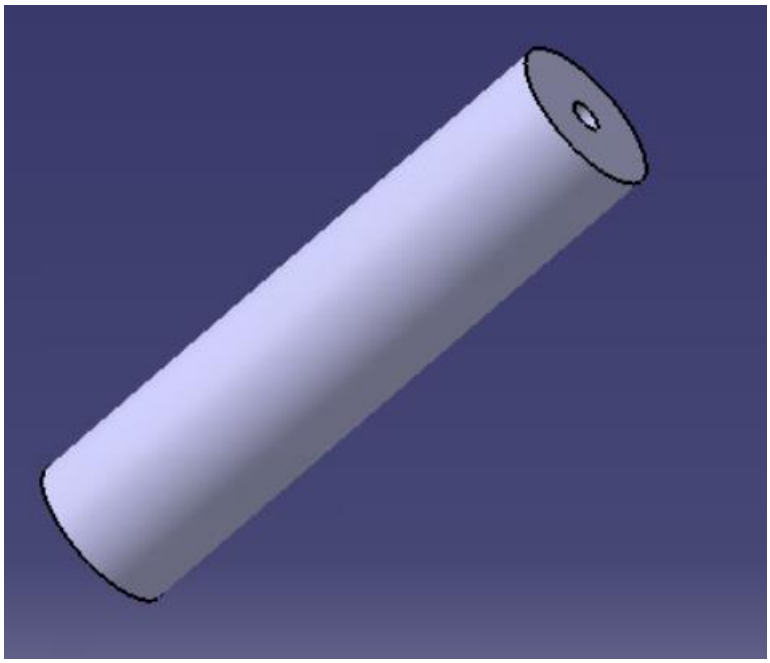

Figure 7.22: Output pins stage 1.

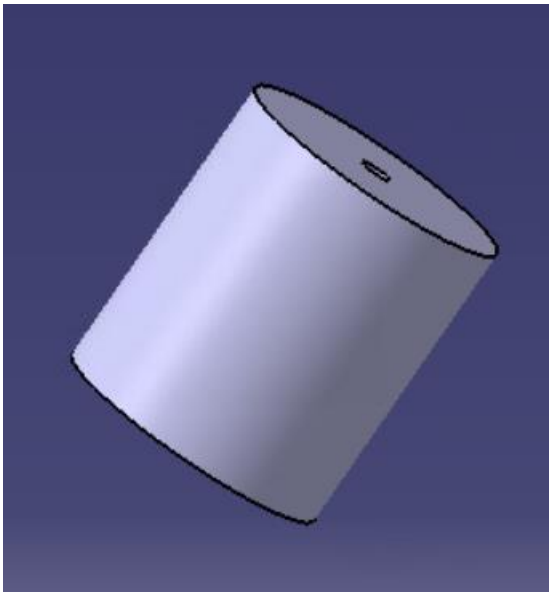

Figure 7.23: Output pins stage 2.

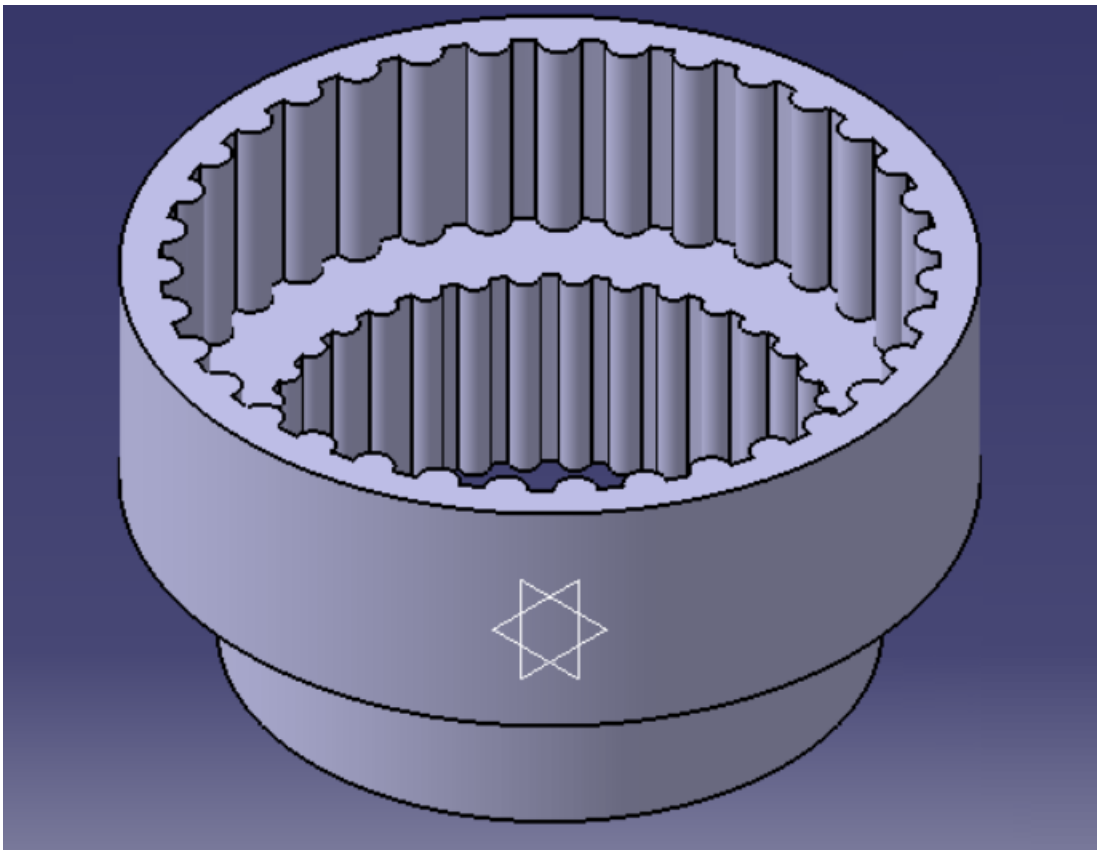

Figure 7.24: Isometric view of cycloidal housing.

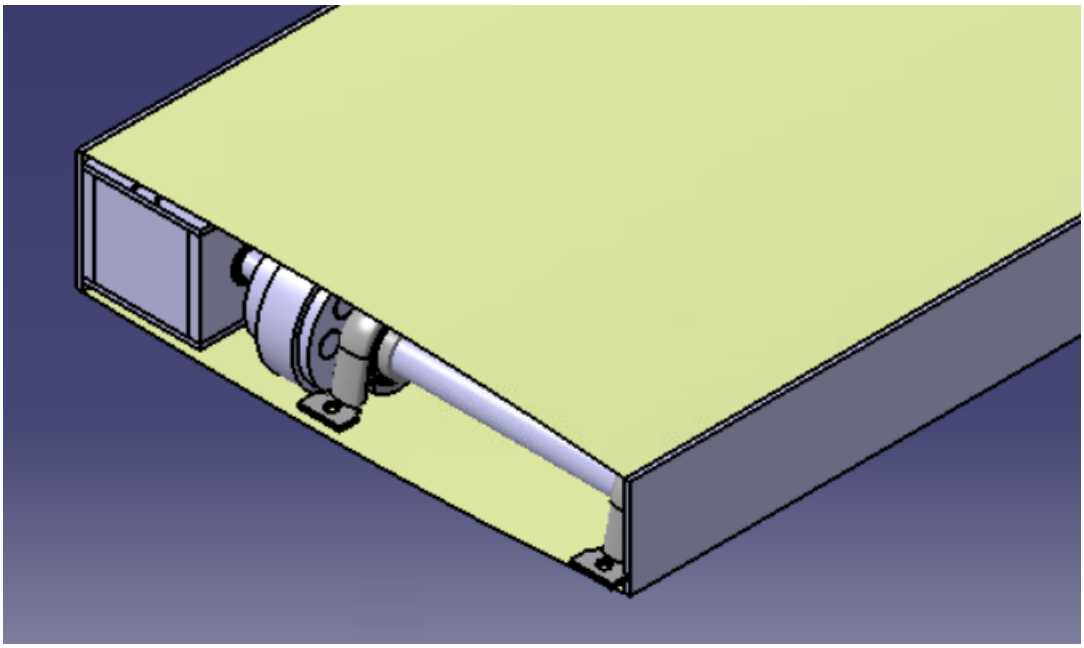

Figure 7.25: Cycloidal drive assembly inside wingbox with all boundaries.

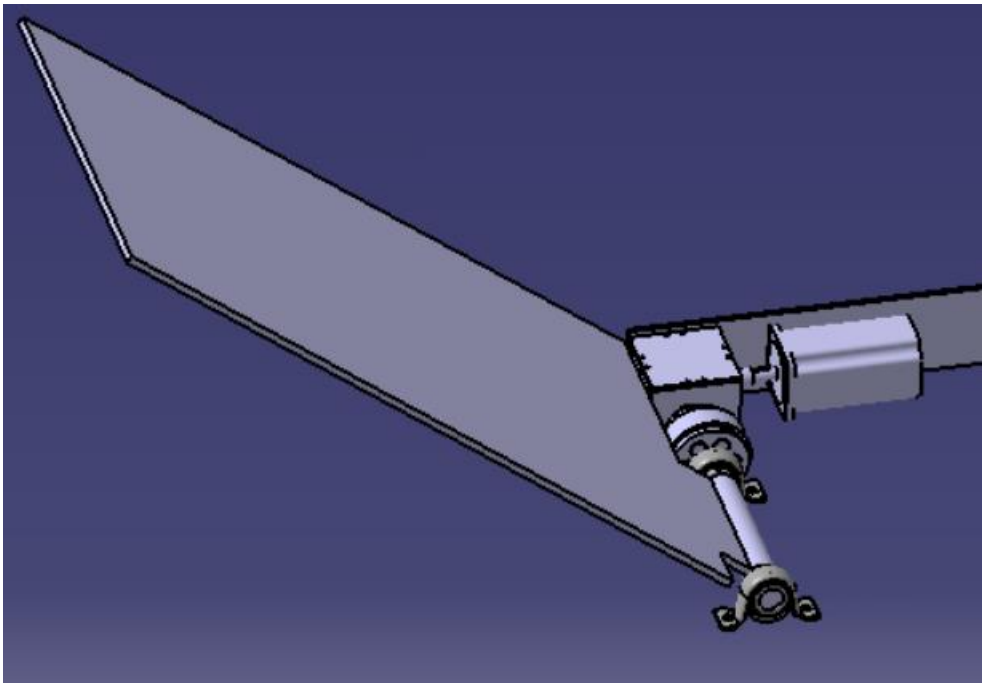

Figure 7.26: Cycloidal drive with winglet.

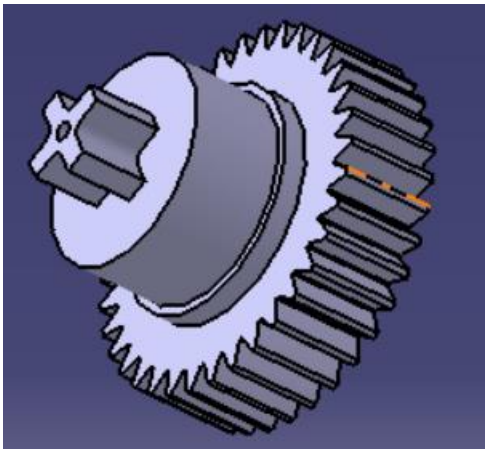

Figure 7.27: Stage one planet gear.

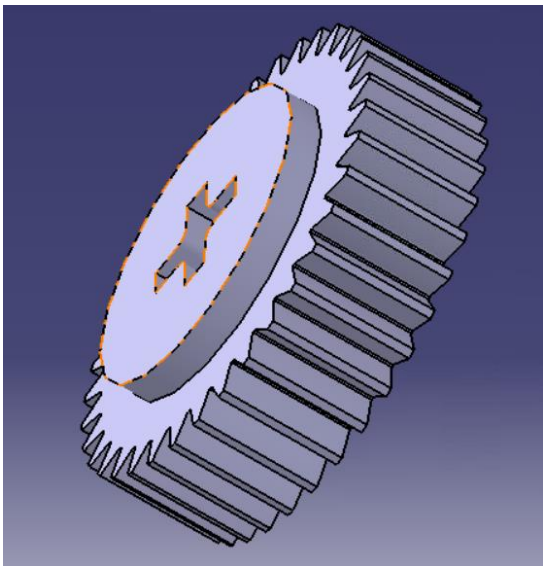

Figure 7.28: Stage two planet gear.

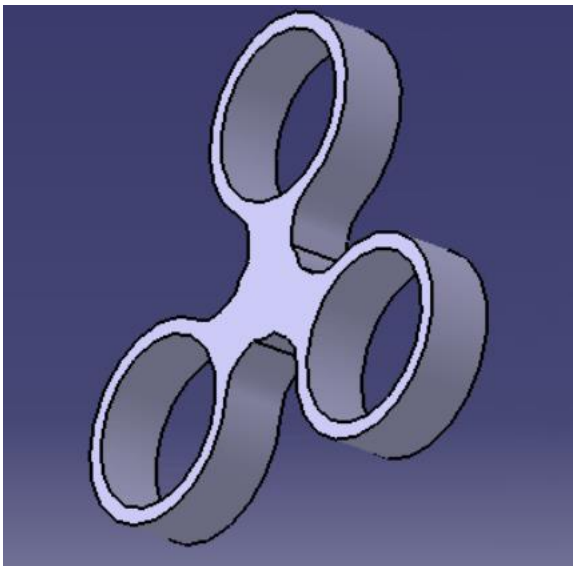

Figure 7.29: Cage.